SMAI-JCM
SMAI Journal of Computational Mathematics

A low-degree strictly conservative finite element method for incompressible flows on general triangulations

Huilan Zeng, Chen-Song Zhang & Shuo Zhang

Volume 8 (2022), p. 225-248.
https://doi.org/10.5802/smai-jcm.85

The SMAI Journal of Computational Mathematics is a member of the Centre Mersenne for Open Scientific Publishing
http://www.centre-mersenne.org/
Submissions at https://smai-jcm.centre-mersenne.org/ojs/submission
e-ISSN: 2426-8399

SMAI Journal of Computational Mathematics
Vol. 8, 225-248 (2022)

A low-degree strictly conservative finite element method for incompressible flows on general triangulations

Huilan Zeng [1]
Chen-Song Zhang [2]
Shuo Zhang [3]

[1] LSEC, Institute of Computational Mathematics and Scientific/Engineering Computation, Academy of Mathematics and System Science, Chinese Academy of Sciences, Beijing 100190, China; University of Chinese Academy of Sciences, Beijing 100049, China
E-mail address: zhl@lsec.cc.ac.cn
[2] LSEC, Institute of Computational Mathematics and Scientific/Engineering Computation, Academy of Mathematics and System Science, Chinese Academy of Sciences, Beijing 100190, China; University of Chinese Academy of Sciences, Beijing 100049, China
E-mail address: zhangcs@lsec.cc.ac.cn
[3] LSEC, Institute of Computational Mathematics and Scientific/Engineering Computation, Academy of Mathematics and System Science, Chinese Academy of Sciences, Beijing 100190, China; University of Chinese Academy of Sciences, Beijing 100049, China
E-mail address: szhang@lsec.cc.ac.cn.

Abstract. In this study, a new $P_2 - P_1$ finite element pair is proposed for incompressible fluid. For this pair, the discrete inf-sup condition and the discrete Korn's inequality hold for general triangulations. It yields strictly conservative velocity approximations when applied to models of incompressible flows. The convergence rate of the scheme can only be proved to be of suboptimal $\mathcal{O}(h)$ order, though, based on the property of strict conservation, the robust capacity of the pair for incompressible flows is verified theoretically and numerically.

2020 Mathematics Subject Classification. 65N12, 65N30, 76D05.

Keywords. incompressible (Navier–)Stokes equations, Brinkman equations, inf-sup condition, discrete Korn's inequality, strictly conservative scheme, pressure-robust discretization.

1. Introduction

The property of conservation plays a key role in the modeling of many physical systems. For the Stokes problem, for example, if a stable finite element pair can inherit mass conservation, the approximation of the velocity can be independent of the pressure, and the method does not suffer from the locking effect with respect to large Reynolds numbers (cf. [9]). The importance of conservative schemes is also significant in, for example, the nonlinear mechanics [2, 3] and the magnetohydrodynamics [22, 24, 25]. In this study, we focus on the conservative scheme for Stokes-type problems for incompressible flows. As Stokes-type problems are applied widely for not only fluid problems but also elastic models, such as the earth model with a fluid core [14], they are immediately connected to many other model problems. Therefore, their conservative schemes can be relevant and helpful for other equations.

Most classical stable Stokes pairs relax the divergence-free constraint by enforcing the condition in the weak sense, and the conservation can be preserved strictly only for special examples. However, during the past decade, conservative schemes have been recognized more clearly as *pressure robustness* and

This work is supported by the Strategic Priority Research Program of Chinese Academy of Sciences (XDB 41000000), National Key R&D Program of China (2020YFA0711904), and the Natural Science Foundation of China (11871465 and 11971472).
https://doi.org/10.5802/smai-jcm.85

have been widely studied and surveyed in [17, 20, 27, 35]. This conservation is also connected to other key features, such as "viscosity-independent" features [39] and "gradient-robustness" features [30] for numerical schemes. There have been various successful examples using different technical approaches. Efforts have been devoted to the construction of conforming conservative pairs, but extra structural assumptions are generally needed for the subdivision and finite element functions. Examples include conforming elements designed for special meshes, such as $P_k - P_{k-1}$ triangular elements for $k \geqslant 4$ on singular-vertex-free meshes [36]; for smaller k values constructed on composite grids [1, 34, 36, 42, 44]; and the pairs given in [15, 20], which work for general triangulations but with an extra smoothness requirement and more complicated shape function spaces. A natural way to relax the constraints is to use $H(\mathrm{div})$-conforming but $(H^1)^2$-nonconforming finite element functions for the velocity. For example, in [32], a reduced cubic polynomial space that is $H(\mathrm{div})$-conforming and $(H^1)^2$-nonconforming was used for the velocity and piecewise constant for the pressure, and the pair was both stable and conservative on general triangulations. The velocity space of [32] can be recognized as modifying an $H(\mathrm{div})$-conforming space by adding some normal bubble-like functions to enforce weak continuity of the tangential component. Several sequel conservative pairs were constructed in [28, 38, 40]. Generally, to construct a conservative pair that works on general triangulations without special structures, cubic and higher-degree polynomials are used for the velocity. In addition, for conservative pairs in three-dimension, we refer to [21, 43, 46], where composite grids were required, as well as [19] and [45], where high-degree local polynomials were utilized. Besides, we also refer to [11, 26, 47] for rectangular grids and [33] for cubic grids, where full advantage was taken of the geometric symmetry of the cells.

In this study, we propose a new $P_2 - P_1$ finite element pair on triangulations; for the velocity field, we use piecewise quadratic $H(\mathrm{div})$ functions whose tangential component is continuous in the average sense, and for the pressure, we use discontinuous piecewise linear functions. The pair is stable and immediately strictly conservative on general triangulations. Further, a discrete Korn's inequality holds for the velocity. The capability of the pair is verified both theoretically and numerically. When applied to the Stokes and the Darcy–Stokes–Brinkman problems, the approximation of the velocity is independent of the small parameters and thus locking-free; numerical experiments verify the validity of the theory. As the tangential component of the velocity function is continuous only in the average sense, the convergence rate can only be proved to be of suboptimal $\mathcal{O}(h)$ order. However, as the pair is conservatively stable on general triangulations, it may play superior to some $\mathcal{O}(h^2)$ nonconservative schemes numerically in robustness with respect to triangulations and small parameters. The performance of the pair on the Navier–Stokes equation is also illustrated numerically. More applications in other model problems for both the source problems and the eigenvalue problems may be studied in the future.

The method given uses an $H(\mathrm{div})$-conforming and $(H^1)^2$-nonconforming finite element for the velocity. Indeed, the space given here is a reduced subspace of the second-order Brezzi–Douglas–Marini element [8] space by enhancing smoothness. This way, the proposed pair is different from most existing $H(\mathrm{div})$ conforming and $(H^1)^2$ nonconforming methods, which propose to add bubble-like basis functions on a specific $H(\mathrm{div})$ finite element space. Moreover, as we use quadratic polynomials only for velocity, to the best of our knowledge, this is the lowest-degree conservative stable pair for the Stokes problem on general triangulations. On the other hand, for the newly designed space for velocity, all the degrees of freedom are located on the edges of the triangulation. It is thus impossible to construct a commutative nodal interpolator with a non-piecewise-constant pressure space. To prove the inf-sup condition, we adopt Stenberg's macroelement technique [37], with a nonstandard macroelement that consists of three sequential triangles. More stable and conservative pairs may be designed by reducing other $H(\mathrm{div})$-conforming elements. The possible generalization of the proposed pair to the three-dimensional case will also be discussed.

Finally, in addition to the finite element methods mentioned above, an alternative is to construct specially discrete variational forms onto $H(\mathrm{div})$ functions where extra stabilizations may play roles;

works such as the discontinuous Galerkin method, the weak Galerkin method, and the virtual element method all fall into this category. There have been many valuable works of these types, but we do not seek to give a complete survey of them and thus will not discuss them in the present paper. Natural connections between the proposed pair and DG-type methods may be expected under the framework of [23]; along the lines of [4], these connections may be helpful for the construction of optimal solvers for DG schemes.

The rest of the study is organized as follows. In the remainder of this section, some notations are given. In Section 2, a new $P_2 - P_1$ element method is proposed, and its significant properties are presented. In Section 3, the convergence analysis of the element applied to the Stokes problem and the Darcy–Stokes–Brinkman problem is provided. In Section 4, numerical experiments are presented to reflect the efficiency of the strictly conservative method when compared with some classical elements.

1.1. **Notations**

Throughout this study, Ω is a bounded and connected polygonal domain in $\mathbb{R}^2$. We use ∇, Δ, div, rot, and curl to denote the gradient, Laplace, divergence, rotation, and curl operators, respectively. As usual, we use $L^p(\Omega)$, $H^s(\Omega)$, $H(\mathrm{div}\,\Omega)$, $H(\mathrm{rot},\Omega)$, $H_0^s(\Omega)$, and $H_0(\mathrm{div}\,\Omega)$ for standard Sobolev spaces. We denote $\underset{\sim}{L}_0^2(\Omega) := \{w \in L^2(\Omega) : \int_\Omega w \,\mathrm{d}\Omega = 0\}$. We use "$\underset{\sim}{\ }$" for vector-valued quantities. Specifically, we denote $\underset{\sim}{L}^p(\Omega) := (L^p(\Omega))^2$ and $\underset{\sim}{H}^s(\Omega) := (H^s(\Omega))^2$. We denote, by $H^{-s}(\Omega)$ and $\underset{\sim}{H}^{-s}(\Omega)$, the dual spaces of $H_0^s(\Omega)$ and $\underset{\sim}{H}_0^s(\Omega)$, respectively. We utilize the subscript "$\cdot_h$" to indicate the dependence on grids. Particularly, an operator with the subscript "$\cdot_h$" implies that the operation is done cell by cell. We denote $(\,\cdot\,,\cdot\,)$ and $\langle\,\cdot\,,\cdot\,\rangle$ as the usual inner product and the dual product, respectively. Finally, $\lesssim$, $\gtrsim$, and $\eqsim$ denote $\leqslant$, $\geqslant$, and $=$, respectively, up to some multiplicative generic constant [41], which only depends on the domain and the shape regularity of subdivisions.

Let $\{\mathcal{T}_h\}$ be in a family of triangular grids of domain Ω. The boundary $\partial\Omega = \Gamma_D \cup \Gamma_N$. Let $\mathcal{N}_h$ be the set of all vertices, $\mathcal{N}_h = \mathcal{N}_h^i \cup \mathcal{N}_h^b$, with $\mathcal{N}_h^i$ and $\mathcal{N}_h^b$ being the interior vertices and the boundary vertices, respectively. Similarly, let $\mathcal{E}_h = \mathcal{E}_h^i \cup \mathcal{E}_h^b$ be the set of all the edges, with $\mathcal{E}_h^i$ and $\mathcal{E}_h^b$ being the interior edges and the boundary edges, respectively. For an edge, e, $\mathbf{n}_e$ is a unit vector normal to e and $\boldsymbol{t}_e$ is a unit tangential vector of e such that $\mathbf{n}_e \times \boldsymbol{t}_e > 0$. On e, we use $[\![\,\cdot\,]\!]_e$ for the jump across e. We stipulate that if $e = T_1 \cap T_2$, then $[\![v]\!]_e = (v|_{T_1} - v|_{T_2})|_e$ if the direction of $\mathbf{n}_e$ goes from T_1 to T_2, and if $e \subset \partial\Omega$, then $[\![\,\cdot\,]\!]_e$ is the evaluation on e.

Suppose that T represents a triangle in $\mathcal{T}_h$. Let h_T and ρ_T be the circumscribed radius and the inscribed circles radius of T, respectively. Let $h := \max_{T\in\mathcal{T}_h} h_T$ be the mesh size of $\mathcal{T}_h$. Let $P_l(T)$ denote the space of polynomials on T of a total degree of no more than l. Similarly, we define the space $P_l(e)$ on e. We assume that $\{\mathcal{T}_h\}$ is a family of regular subdivisions; that is,

$$\max_{T\in\mathcal{T}_h} \frac{h_T}{\rho_T} \leqslant \gamma_0, \tag{1.1}$$

where γ_0 is a generic constant independent of h.

2. **A new $P_2 - P_1$ finite element pair**

2.1. **Construction of a new finite element pair**

Let T be a triangle with nodes $\{a_1, a_2, a_3\}$(counterclockwise), and e_i be an edge of T opposite to a_i, $i = 1, 2, 3$; see Figure 2.1. Denote a unit outer normal vector of e_i and a unit tangential vector of e_i as $\mathbf{n}_{T,e_i}$ and $\mathbf{t}_{T,e_i}$, respectively, such that $\mathbf{n}_{T,e_i} \times \mathbf{t}_{T,e_i} = 1$. Let λ_i, $i = 1, 2, 3$, denote the barycentric coordinates.

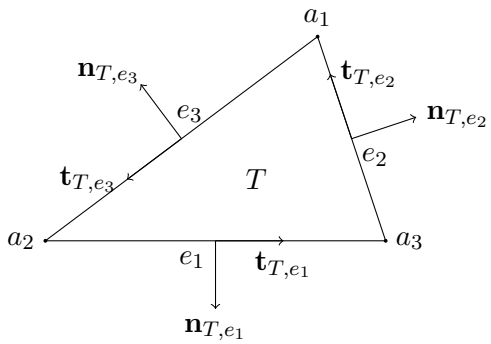

FIGURE 2.1. Illustration of a triangle and its nodes and edges.

The new vector P_2 element is defined by the triple (T, P_T, D_T):

(1) T is a triangle;

(2) $P_T := (P_2(T))^2$;

(3) for any $\underset{\sim}{v} \in (H^1(T))^2$, the degrees of freedom on T, denoted by D_T, are

$$D_T := \left\{ \begin{array}{l} \mathbf{d}_{\mathbf{n}_{T,e_i},0}(\underset{\sim}{v}) = \fint_{e_i} \underset{\sim}{v} \cdot \mathbf{n}_{T,e_i}\,\mathrm{d}s,\ \mathbf{d}_{\mathbf{n}_{T,e_i},1}(\underset{\sim}{v}) = \fint_{e_i} \underset{\sim}{v} \cdot \mathbf{n}_{T,e_i}(\lambda_j - \lambda_k)\,\mathrm{d}s, \\ \mathbf{d}_{\mathbf{n}_{T,e_i},2}(\underset{\sim}{v}) = \fint_{e_i} \underset{\sim}{v} \cdot \mathbf{n}_{T,e_i}(-\lambda_j\lambda_k + \frac{1}{6})\,\mathrm{d}s,\ \mathbf{d}_{\mathbf{t}_{T,e_i},0}(\underset{\sim}{v}) = \fint_{e_i} \underset{\sim}{v} \cdot \mathbf{t}_{T,e_i}\,\mathrm{d}s, \\ \qquad\qquad\qquad\qquad\qquad\qquad\qquad\qquad i = 1,2,3,\ \{i,j,k\} = \{1,2,3\} \end{array} \right\}. \tag{2.1}$$

The above triple is P_T-unisolvent. Particularly, we denote

$$\left\{ \begin{array}{l} \underset{\sim}{\varphi}_{\mathbf{n}_{T,e_i},0} = \lambda_j(3\lambda_j - 2)\dfrac{\mathbf{t}_{T,e_k}}{(\mathbf{n}_{T,e_i}, \mathbf{t}_{T,e_k})} + \lambda_k(3\lambda_k - 2)\dfrac{\mathbf{t}_{T,e_j}}{(\mathbf{n}_{T,e_i}, \mathbf{t}_{T,e_j})} + 6\lambda_j\lambda_k\mathbf{n}_{T,e_i}; \\ \underset{\sim}{\varphi}_{\mathbf{n}_{T,e_i},1} = 3\lambda_j(3\lambda_j - 2)\dfrac{\mathbf{t}_{T,e_k}}{(\mathbf{n}_{T,e_i}, \mathbf{t}_{T,e_k})} - 3\lambda_k(3\lambda_k - 2)\dfrac{\mathbf{t}_{T,e_j}}{(\mathbf{n}_{T,e_i}, \mathbf{t}_{T,e_j})}; \\ \underset{\sim}{\varphi}_{\mathbf{n}_{T,e_i},2} = 30\lambda_j(3\lambda_j - 2)\dfrac{\mathbf{t}_{T,e_k}}{(\mathbf{n}_{T,e_i}, \mathbf{t}_{T,e_k})} + 30\lambda_k(3\lambda_k - 2)\dfrac{\mathbf{t}_{T,e_j}}{(\mathbf{n}_{T,e_i}, \mathbf{t}_{T,e_j})}; \\ \underset{\sim}{\varphi}_{\mathbf{t}_{T,e_i},0} = 6\lambda_j\lambda_k\mathbf{t}_i. \end{array} \right. \tag{2.2}$$

Then,

$$\mathbf{d}_{\mathbf{n}_{T,e_i},k}(\underset{\sim}{\varphi}_{\mathbf{n}_{T,e_j},l}) = \delta_{ij}\delta_{kl}, \quad \mathbf{d}_{\mathbf{n}_{T,e_i},k}(\underset{\sim}{\varphi}_{\mathbf{t}_{T,e_j},0}) = 0, \quad \mathbf{d}_{\mathbf{t}_{T,e_i},0}(\underset{\sim}{\varphi}_{\mathbf{n}_{T,e_j},k}) = 0,$$
$$\text{and} \quad \mathbf{d}_{\mathbf{t}_{T,e_i},0}(\underset{\sim}{\varphi}_{\mathbf{t}_{T,e_j},0}) = \delta_{ij},\ i,j,k,l = 1,2,3. \tag{2.3}$$

Note that if e is shared by two triangles T_1 and T_2, then

$$\left\{ \begin{array}{l} \mathbf{d}_{\mathbf{n}_{T_1},e,0}(\underset{\sim}{v}) = -\mathbf{d}_{\mathbf{n}_{T_2},e,0}(\underset{\sim}{v}),\ \mathbf{d}_{\mathbf{n}_{T_1},e,2}(\underset{\sim}{v}) = -\mathbf{d}_{\mathbf{n}_{T_2},e,2}(\underset{\sim}{v}),\ \mathbf{d}_{\mathbf{t}_{T_1},e,0}(\underset{\sim}{v}) = -\mathbf{d}_{\mathbf{t}_{T_2},e,0}(\underset{\sim}{v}), \\ \text{but}\ \ \mathbf{d}_{\mathbf{n}_{T_1},e,1}(\underset{\sim}{v}) = \mathbf{d}_{\mathbf{n}_{T_2},e,1}(\underset{\sim}{v}), \end{array} \right. \tag{2.4}$$

for any function $\underset{\sim}{v}$ that is integrable on e.

The corresponding finite element space is defined by

$$\underset{\sim}{V}_h := \left\{ \underset{\sim}{v}_h \in \underset{\sim}{L}^2(\Omega) : \begin{array}{l} \underset{\sim}{v}_h|_T \in (P_2(T))^2,\ \forall\, T \in \mathcal{T}_h;\ \ \underset{\sim}{v}_h \cdot \mathbf{n}_e \\ \text{and}\ \fint_e \underset{\sim}{v}_h \cdot \mathbf{t}_e\,\mathrm{d}s \text{ are continuous across } e \in \mathcal{E}_h^i \end{array} \right\}.$$

Note that $\underset{\sim}{V}_h \subset \underset{\sim}{H}(\operatorname{div}\Omega)$ but $\underset{\sim}{V}_h \not\subset \underset{\sim}{H}^1(\Omega)$.

We define a nodal interpolation operator $\Pi_h : \underset{\sim}{H}^1(\Omega) \to \underset{\sim}{V}_h$ such that for any $e \in \mathcal{E}_h$,

$$\fint_e \Pi_h \underset{\sim}{v} \cdot \mathbf{n}_e \, w \, \mathrm{d}s = \fint_e \underset{\sim}{v} \cdot \mathbf{n}_e \, w \, \mathrm{d}s, \quad \forall\, w \in P_2(e),$$
$$\fint_e \Pi_h \underset{\sim}{v} \cdot \mathbf{t}_e \, \mathrm{d}s = \fint_e \underset{\sim}{v} \cdot \mathbf{t}_e \, \mathrm{d}s.$$

The operator Π_h is locally defined, and the local space $\underset{\sim}{V}_h(T)$, restricted on T, is invariant under Piola's transformation; that is, it maps $\underset{\sim}{V}_h(T)$ onto $\underset{\sim}{V}_h(\widehat{T})$, where $\widehat{T}$ represents a reference triangle. Moreover, Π_h preserves quadratic functions locally. Therefore, a combination of Lemmas 1.6 and 1.7 in [9], standard scaling arguments, and the Bramble–Hilbert lemma leads to the following approximation property of Π_h.

Proposition 2.1. *If $0 \leqslant k \leqslant 1 \leqslant s \leqslant 3$, then*

$$|\underset{\sim}{v} - \Pi_h \underset{\sim}{v}|_{k,h} \lesssim h^{s-k} |\underset{\sim}{v}|_{s,\Omega}, \quad \forall\, \underset{\sim}{v} \in \underset{\sim}{H}^s(\Omega). \tag{2.5}$$

Moreover, the following low-order estimate is valid:

$$\|\underset{\sim}{v} - \Pi_h \underset{\sim}{v}\|_{0,\Omega} \lesssim h^{1/2} \|\underset{\sim}{v}\|_{0,\Omega} \|\underset{\sim}{v}\|_{1,\Omega}. \tag{2.6}$$

Assume Γ_D to be a part of the boundary $\partial\Omega$. We define

$$\underset{\sim}{V}_{hD} := \left\{ \begin{array}{c} \underset{\sim}{v}_h|_T \in (P_2(T))^2, \ \forall\, T \in \mathcal{T}_h; \\ \underset{\sim}{v}_h \in \underset{\sim}{L}^2(\Omega) : \underset{\sim}{v}_h \cdot \mathbf{n}_e \text{ and } \fint_e \underset{\sim}{v}_h \cdot \mathbf{t}_e \, \mathrm{d}s \text{ are continuous} \\ \text{for any } e \in \mathcal{E}_h^i \text{ and vanish for any } e \subset \Gamma_D \end{array} \right\}.$$

Specially, if $\Gamma_D = \partial\Omega$, $\underset{\sim}{V}_{hD}$ is written as $\underset{\sim}{V}_{h0}$. We define

$$Q_h := \{q \in L^2(\Omega) : q|_T \in P_1(T), \forall\, T \in \mathcal{T}_h\}, \quad \text{and} \quad Q_{h*} := Q_h \cap L_0^2(\Omega).$$

Evidently, $\operatorname{div} \underset{\sim}{V}_h \subset Q_h$. Therefore, $\underset{\sim}{V}_{hD} \times Q_h$ and $\underset{\sim}{V}_{h0} \times Q_{h*}$ each forms a conservative pair. The stability and discrete Korn's inequality also hold. We first introduce an assumption on the triangulations.

Assumption A. *Every triangle in $\mathcal{T}_h$ has at least one vertex in the interior of Ω.*

The theorems below, which will be proved in the sequel subsections, hold for triangulations that satisfy Assumption A.

Theorem 2.2 (Inf-sup conditions)**.** *Let $\{\mathcal{T}_h\}$ be a family of triangulations satisfying Assumption A. Then,*

$$\sup_{\underset{\sim}{v}_h \in \underset{\sim}{V}_{hD}} \frac{\int_\Omega \operatorname{div} \underset{\sim}{v}_h \, q_h \, \mathrm{d}\Omega}{\|\underset{\sim}{v}_h\|_{1,h}} \gtrsim \|q\|_{0,\Omega}, \quad \forall\, q \in Q_h, \quad \textit{if } \ \Gamma_D \neq \partial\Omega, \tag{2.7}$$

$$\sup_{\underset{\sim}{v}_h \in \underset{\sim}{V}_{h0}} \frac{\int_\Omega \operatorname{div} \underset{\sim}{v}_h \, q_h \, \mathrm{d}\Omega}{\|\underset{\sim}{v}_h\|_{1,h}} \gtrsim \|q\|_{0,\Omega}, \quad \forall\, q \in Q_{h*}. \tag{2.8}$$

Theorem 2.3 (Discrete Korn's inequality)**.** *Let $\epsilon(\underset{\sim}{v}) := \frac{1}{2}[\nabla v + (\nabla v)^T]$. Then*

$$\sum_{T \in \mathcal{T}_h} \int_T |\epsilon(\underset{\sim}{v})|^2 \, \mathrm{d}T \gtrsim |\underset{\sim}{v}|_{1,h}^2, \quad \forall\, \underset{\sim}{v} \in \underset{\sim}{V}_{hD}. \tag{2.9}$$

2.2. **Proof of inf-sup conditions**

Note that the commutativity $\operatorname{div}\Pi_h \underset{\sim}{w} = P_{Q_{h*}} \operatorname{div} \underset{\sim}{w}$ does not hold for all $\underset{\sim}{w} \in \underset{\sim}{H}{}^1_0(\Omega)$, where $P_{Q_{h*}}$ represents the L^2 projection onto Q_{h*}. To prove the inf-sup conditions (2.7) and (2.8), we adopt the macroelement technique by Stenberg [37]. We postpone the proof of Theorem 2.2 after some technical preparations.

2.2.1. *Stenberg's macroelement technique*

A macroelement is a connected set of at least two cells in $\mathcal{T}_h$. A macroelement partition of $\mathcal{T}_h$, denoted by $\mathcal{M}_h$, is a set of macroelements such that each triangle in of $\mathcal{T}_h$ is covered by at least one macroelement in $\mathcal{M}_h$.

Definition 2.4. Two macroelements, M_1 and M_2, are said to be equivalent if there exists a continuous one-to-one mapping of $G:\ M_1 \to M_2$, such that

(a) $G(M_1) = M_2$;

(b) if $M_1 = \bigcup_{i=1}^m T_i^1$, then $T_i^2 = G(T_i^1)$ with $i = 1 : m$ are the cells of M_2.

(c) $G|_{T_i^1} = F_{T_i^2} \circ F_{T_i^1}^{-1}$, $i = 1 : m$, where $F_{T_i^1}$ and $F_{T_i^2}$ are the mappings from a reference element $\widehat{T}$ onto T_i^1 and T_i^2, respectively.

A class of equivalent macroelements is a set of all the macroelements that are equivalent to each other. Given a macroelement, M, viewed as a special triangulation, we denote

$$\underset{\sim}{V}_{h0,M} := \underset{\sim}{V}_{h0} \text{ on } M, \quad Q_{h,M} := Q_h \text{ on } M, \quad \text{and} \quad Q_{h*,M} := Q_{h*} \text{ on } M.$$

Moreover, we denote

$$N_M := \left\{ q_h \in Q_{h,M} :\ \int_M \operatorname{div} \underset{\sim}{v}_h\ q_h \,\mathrm{d}M = 0,\ \forall\, \underset{\sim}{v}_h \in \underset{\sim}{V}_{h0,M} \right\}. \tag{2.10}$$

Stenberg's macroelement technique can be summarized as the following proposition.

Proposition 2.5 ([37, Theorem 3.1])**.** *Suppose there exists a macroelement partitioning, $\mathcal{M}_h$, with a fixed set of equivalence classes $\mathbb{E}_i$ of macroelements, $i = 1,\ 2,\ \ldots,\ n$, a positive integer N (n and N are independent of h), and an operator $\Pi : \underset{\sim}{H}{}^1_0(\Omega) \to \underset{\sim}{V}_{h0}$. Then,*

(C_1) *for each $M \in \mathbb{E}_i$, $i = 1,\ 2,\ \ldots,\ n$, the space N_M defined in* (2.10) *is one-dimensional, which consists of functions that are constant on M;*

(C_2) *each $M \in \mathcal{M}_h$ belongs to one of the classes $\mathbb{E}_i$, $i = 1,\ 2,\ \ldots,\ n$;*

(C_3) *each $e \in \mathcal{E}_h^i$ is an interior edge of at least one and no more than N macroelements;*

(C_4) *for any $\underset{\sim}{w} \in \underset{\sim}{H}{}^1_0(\Omega)$, it holds that*

$$\sum_{T\in\mathcal{T}_h} h_T^{-2}\|\underset{\sim}{w} - \Pi\underset{\sim}{w}\|_{0,T}^2 + \sum_{e\in\mathcal{E}_h^i} h_e^{-1}\|\underset{\sim}{w} - \Pi\underset{\sim}{w}\|_{0,e}^2 \lesssim \|\underset{\sim}{w}\|_{1,\Omega}^2 \quad \textit{and} \quad \|\Pi\underset{\sim}{w}\|_{1,h} \lesssim \|\underset{\sim}{w}\|_{1,\Omega}.$$

Then, the stability (2.8) *is valid.*

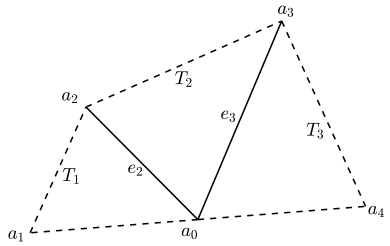

FIGURE 2.2. Macroelement by three sequential triangles, T_1, T_2, and T_3.

2.2.2. *Technical lemmas*

In general, the main difficulty to design a stable mixed element stems from (C_1). We use the specific type of macroelements as below.

Definition 2.6. A macroelement, denoted by M, is the union of the three sequential cells connected by two shared edges. (See Figure 2.2 for a reference.)

Below are concrete definitions of some local defined spaces on M introduced in the previous context.

$$\underset{\sim}{V}_{h0,M} := \left\{ \underset{\sim}{v}_h \in \underset{\sim}{L}^2(M) : \begin{array}{l} \underset{\sim}{v}_h|_T \in (P_2(T))^2, \forall\, T \subset M,\ \underset{\sim}{v}_h \cdot \mathbf{n}_e \text{ and } \fint_e \underset{\sim}{v}_h \cdot \mathbf{t}_e \,\mathrm{d}s \text{ are} \\ \text{continuous across interior edges and vanish on } \partial M \end{array} \right\},$$

$$Q_{h,M} = \Big\{ q_h \in L^2(M) : q_h|_T \in P_1(T),\ \forall\, T \subset M \Big\},$$

$$Q_{h*,M} = \left\{ q_h \in Q_{h,M} : \int_M q_h \,\mathrm{d}M = 0 \right\}.$$

Denote $\ker(\operatorname{div} \underset{\sim}{V}_{h0,M}) := \{\underset{\sim}{v}_h \in \underset{\sim}{V}_{h0,M} : \operatorname{div} \underset{\sim}{v}_h = 0\}$ and $\operatorname{Im}(\operatorname{div} \underset{\sim}{V}_{h0,M}) = \operatorname{div}(\underset{\sim}{V}_{h0,M})$. The crucial lemma below makes this study different from general macroelement argument.

Lemma 2.7. $\ker(\operatorname{div} \underset{\sim}{V}_{h0,M}) = \{0\}$.

Proof. We begin with the detailed structure of the space of divergence-free functions. Let T be a triangle with nodes $\{a_i, a_j, a_k\}$ (counterclockwise) and edges $\{e_i, e_j, e_k\}$ opposite to $\{a_i, a_j, a_k\}$, respectively. Denote $\mathbf{n}_{T,e_m}$ as the unit outward normal vector of e_m and $\mathbf{t}_{T,e_m}$ as a unit tangential vector of e_m such that $\mathbf{n}_{T,e_m} \times \mathbf{t}_{T,e_m} > 0$, $m \in \{i,\ j,\ k\}$. Denote the lengths of edges by $\{l_i, l_j, l_k\}$, and the area of T by S.

FIGURE 2.3. Degrees of freedom vanish on dotted edges.

Denote

$$\underset{\sim}{W}_{T,e_je_k} := \left\{ \underset{\sim}{v} \in (P_2(T))^2 : \operatorname{div} \underset{\sim}{v} = 0,\ \int_{e_i} \underset{\sim}{v} \cdot \mathbf{t}_{e_i} = 0, \int_{e_i} \underset{\sim}{v} \cdot \mathbf{n}_{e_i} q = 0,\ \forall\, q \in P_2(e_i) \right\}. \tag{2.11}$$

Namely, $\underset{\sim}{W}_{T,e_je_k}$ consists of vector quadratic polynomials that are divergence-free, and the nodal parameters associated with e_i are equal to zero. Then, $\dim(\underset{\sim}{W}_{T,e_je_k}) = 5$. Indeed, it is easy to see

curl is a bijection from $\{\psi \in P_3(T) : \psi|_{e_i} = 0,\ \int_{e_i} \frac{\partial \psi}{\partial \mathbf{n}_{e_i}} = 0\}$ onto $\underset{\sim}{W}_{T,e_je_k}$. Further, $\{\psi \in P_3(T) : \psi|_{e_i} = 0,\ \int_{e_i} \frac{\partial \psi}{\partial \mathbf{n}_{e_i}} = 0\} = \{\lambda_i \cdot p : p \in P_2(T),\ \int_{e_i} \frac{\partial \lambda_i \cdot p}{\partial \mathbf{n}_{e_i}} = 0\} = \{\lambda_i \cdot p : p \in P_2(T), \int_{e_i} p = 0\}$, and $\dim(\underset{\sim}{W}_{T,e_je_k}) = \dim(\{p \in P_2(T) : \int_{e_i} p = 0\}) = 5$.
Now, let $\underset{\sim}{\varphi}'s$ be the basis functions given in (2.2). We can simply calculate the divergence of the functions and record them into Table 2.1:

TABLE 2.1. Divergence of basis functions of (2.2)

$\underset{\sim}{\varphi}$	$\underset{\sim}{\varphi}_{T,\mathbf{n}_j,0}$	$\underset{\sim}{\varphi}_{T,\mathbf{n}_j,1}$	$\underset{\sim}{\varphi}_{T,\mathbf{n}_j,2}$	$\underset{\sim}{\varphi}_{T,\mathbf{t}_j,0}$
$\int_T \operatorname{div}(\underset{\sim}{\varphi})\ \lambda_i$	$\frac{3l_i^2-11l_j^2-3l_k^2}{24l_j}$	$\frac{3l_j}{4}$	$-15l_j$	$\frac{S}{2l_j}$
$\int_T \operatorname{div}(\underset{\sim}{\varphi})\ \lambda_j$	$\frac{-l_j}{12}$	0	$5l_j$	0
$\int_T \operatorname{div}(\underset{\sim}{\varphi})\ \lambda_k$	$\frac{-3l_i^2-11l_j^2+3l_k^2}{24l_j}$	$\frac{-3l_j}{4}$	$\frac{-5l_j}{2}$	$\frac{-S}{2l_j}$

By solving a 8×3 linear system, generated based on the data of Table 2.1, we can explicitly construct the five linearly independent basis functions of $\underset{\sim}{W}_{T,e_je_k}$, which are

$$\underset{\sim}{w}_{T,e_j} = \frac{2S}{3l_j^2}\underset{\sim}{\varphi}_{\mathbf{n}_{T,e_j},1} - \underset{\sim}{\varphi}_{\mathbf{t}_{T,e_j},0}, \qquad \underset{\sim}{w}_{T,e_k} = -\frac{2S}{3l_k^2}\underset{\sim}{\varphi}_{\mathbf{n}_{T,e_k},1} + \underset{\sim}{\varphi}_{\mathbf{t}_{T,e_k},0}, \tag{2.12}$$

$$\begin{aligned} \underset{\sim}{w}_{T,e_j,e_k} &= -\frac{1}{3l_j}\underset{\sim}{\varphi}_{\mathbf{n}_{T,e_j},1} + \frac{1}{10l_j}\underset{\sim}{\varphi}_{\mathbf{n}_{T,e_j},2} - \frac{2}{3l_k}\underset{\sim}{\varphi}_{\mathbf{n}_{T,e_k},1}, \\ \underset{\sim}{w}_{T,e_k,e_j} &= -\frac{2}{3l_j}\underset{\sim}{\varphi}_{\mathbf{n}_{T,e_j},1} - \frac{1}{3l_k}\underset{\sim}{\varphi}_{\mathbf{n}_{T,e_k},1} - \frac{1}{10l_k}\underset{\sim}{\varphi}_{\mathbf{n}_{T,e_k},2}, \end{aligned} \tag{2.13}$$

$$\begin{aligned} \text{and} \quad \underset{\sim}{w}_{T,a_i} = -\frac{1}{l_j}\underset{\sim}{\varphi}_{\mathbf{n}_{T,e_j},0} &+ \frac{-l_i^2l_j^2 + 2l_i^2l_k^2 + l_j^4 + 3l_j^2l_k^2 - 2l_k^4}{12l_j^3l_k^2}\underset{\sim}{\varphi}_{\mathbf{n}_{T,e_j},1} \\ &+ \frac{l_i^2 - l_j^2 + 3l_k^2}{40l_jl_k^2}\underset{\sim}{\varphi}_{\mathbf{n}_{T,e_j},2} + \frac{1}{l_k}\underset{\sim}{\varphi}_{\mathbf{n}_{T,e_k},0}. \end{aligned} \tag{2.14}$$

Namely,

$$\underset{\sim}{W}_{T,e_je_k} = \operatorname{span}\{\underset{\sim}{w}_{T,e_j},\ \underset{\sim}{w}_{T,e_j,e_k},\ \underset{\sim}{w}_{T,e_k,e_j},\ \underset{\sim}{w}_{T,e_k},\ \underset{\sim}{w}_{T,a_i}\}.$$

Particularly, $\underset{\sim}{w}_{T,e_j}$ and $\underset{\sim}{w}_{T,e_k}$ each has vanishing degrees of freedom on two edges.
Now, we turn back to Figure 2.2. Given $\underset{\sim}{w}_M \in \ker(\operatorname{div} \underset{\sim}{V}_{h0,M})$, by the boundary condition on ∂M, $\underset{\sim}{w}_M|_{T_1}$ and $\underset{\sim}{w}_M|_{T_3}$ are both of the (2.12) types. Therefore, by the continuation of degrees of freedom of $\underset{\sim}{w}_M$ across e_2 and e_3, $\underset{\sim}{v}_M|_{T_2}$ does not contain a component along $\underset{\sim}{\varphi}_{\mathbf{n}_{T_2,e_2},0}$, $\underset{\sim}{\varphi}_{\mathbf{n}_{T_2,e_2},2}$, $\underset{\sim}{\varphi}_{\mathbf{n}_{T_2,e_3},0}$ or $\underset{\sim}{\varphi}_{\mathbf{n}_{T_2,e_3},2}$. This implies that $\underset{\sim}{v}_M|_{T_2}$ does not contain a component on $\underset{\sim}{w}_{T_2,a_0}$ (according to $\underset{\sim}{\varphi}_{\mathbf{n}_{T_2,e_2},0}$ and $\underset{\sim}{\varphi}_{\mathbf{n}_{T_2,e_3},0}$), $\underset{\sim}{w}_{T_2,e_2,e_3}$ or $\underset{\sim}{w}_{T_2,e_3,e_2}$ (further according to $\underset{\sim}{\varphi}_{\mathbf{n}_{T_2,e_2},2}$ and $\underset{\sim}{\varphi}_{\mathbf{n}_{T_2,e_3},2}$). This implies that $\underset{\sim}{v}_M|_{T_2}$ consists of functions of the (2.12) type only. However, by the symmetry of nodal parameters across internal edges (cf. (2.4)), the two functions of (2.12) type on T_1 and T_2 cannot satisfy the continuity condition on e_2 unless they are both zero, and so is on e_3. Therefore, $\underset{\sim}{w}_M$ vanishes in the whole macroelement. Thus, the proof is completed. ∎

Lemma 2.8. *For M, a macroelement, the space N_M, defined as* (2.10)*, is a one-dimensional space consisting of constant functions on M.*

Proof. First, we show $\operatorname{Im}(\operatorname{div} \underset{\sim}{V}_{h0,M}) = Q_{h*,M}$. As $\dim(\underset{\sim}{V}_{h0,M}) = \dim(\ker(\operatorname{div} \underset{\sim}{V}_{h0,M})) + \dim(\operatorname{Im}(\operatorname{div} \underset{\sim}{V}_{h0,M}))$, we obtain $\dim(\operatorname{Im}(\operatorname{div} \underset{\sim}{V}_{h0,M})) = \dim(\underset{\sim}{V}_{h0,M}) - \dim(\ker(\operatorname{div} \underset{\sim}{V}_{h0,M})) = 8 - 0 = 8$.

Note that $\dim(Q_{h*,M}) = 3{\cdot}3-1 = 8$ and $\mathrm{Im}(\operatorname{div} \underset{\sim}{V}_{h0,M}) \subset Q_{h*,M}$, so we derive $\mathrm{Im}(\operatorname{div} \underset{\sim}{V}_{h0,M}) = Q_{h*,M}$. Then, for any $q_h \in N_M$, it holds that $\int_M p_h^*\, q_h \,\mathrm{d}M = 0$, for any $p_h^* \in Q_{h*,M}$. Let $q_h = \overline{q}_h + q_h^*$, where $\overline{q}_h = \fint_M q_h \,\mathrm{d}M$ and $q_h^* \in Q_{h*,M}$. Then, $\int_M p_h^*\, q_h^* \,\mathrm{d}M = 0,\ \forall\ p_h^* \in Q_{M,*}$, which yields $q_h^* = 0$, so $q_h = \overline{q}_h$. Therefore, N_M is a one-dimensional space consisting of constant functions on M. The proof is completed. ∎

Lemma 2.9. *Let $\{\mathcal{T}_h\}$ be a family of triangulations satisfying Assumption A. Each macroelement in $\mathcal{M}_h$ has one interior vertex. Then, conditions C_2, C_3, and C_4 in Proposition 2.5 are satisfied.*

Proof. From Assumption A and the regularity (1.1) of $\mathcal{T}_h$, there exists a generic constant, n, independent of h, such that condition C_2 holds. If $e \in \mathcal{E}_h^i$, then at least one endpoint of e is an interior vertex. Hence, e is an interior edge of at least one macroelement of $\mathcal{M}_h$. However, e is interior to at most two macroelements, which occurs if both endpoints of e are interior in Ω. Therefore, the condition C_3 also holds. By Proposition 2.1 and the well-known trace theorem (see, e.g., [6, Theorem 1.6.6]), condition C_4 can be obtained. ∎

2.2.3. *Proof of Theorem 2.2*

Proof of Theorem 2.2. By Lemma 2.8, Lemma 2.9, and Proposition 2.5, it holds that $\underset{\sim}{V}_{h0} \times Q_{h*}$ satisfies the inf-sup condition (2.8). The inf-sup stability of $\underset{\sim}{V}_{hD} \times Q_h$ is proved utilizing the technique introduced in [29] by the following four steps:

Step 1. Given $q_h \in Q_h$, let $\overline{q}_h = \frac{1}{|\Omega|}\int_\Omega q_h \,\mathrm{d}\Omega$ and $q_h^* = q_h - \overline{q}_h$. Then, $q_h^* \in L_0^2(\Omega)$, and

$$\|q_h\|_{0,\Omega}^2 = \|\overline{q}_h\|_{0,\Omega}^2 + \|q_h^*\|_{0,\Omega}^2. \tag{2.15}$$

Step 2. By (2.8), there exists some $\underset{\sim}{v}^* \in \underset{\sim}{V}_{h0}$ such that

$$(\operatorname{div} \underset{\sim}{v}_h^*, q_h^*) \geqslant C_1 \|q_h^*\|_{0,\Omega}^2 \quad \text{and} \quad |\underset{\sim}{v}_h^*|_{1,h} = \|q_h^*\|_{0,\Omega}, \tag{2.16}$$

where $C_1 > 0$ is a generic constant independent of h.

Step 3. Let $\Gamma_N := \partial\Omega \backslash \Gamma_D$. Notice that $\overline{q}_h$ is constant in Ω. Let $\underset{\sim}{\overline{v}}_h \in \underset{\sim}{V}_{hD}$ satisfy that $\underset{\sim}{\overline{v}}_h \cdot \mathbf{n_e} = C_0 \overline{q}_h|_e$ for any $e \subset \Gamma_N$, and other degrees of freedom vanish. The value of C_0 is chosen such that $|\underset{\sim}{\overline{v}}_h|_{1,h} = \|\overline{q}_h\|_{0,\Omega}$. Then, it holds with $C_2 := C_0 \frac{|\Gamma_N|}{|\Omega|}$ that

$$(\operatorname{div} \underset{\sim}{\overline{v}}_h, \overline{q}_h) = \sum_{T\in\mathcal{T}_h} \int_T \operatorname{div} \underset{\sim}{\overline{v}}_h\, \overline{q}_h \,\mathrm{d}T = \sum_{e\in\Gamma_N} \int_e \underset{\sim}{\overline{v}}_h \cdot \mathbf{n}\, \overline{q}_h \,\mathrm{d}s = C_2 \|\overline{q}_h\|_{0,\Omega}^2. \tag{2.17}$$

Step 4. Let $\underset{\sim}{v}_h = \underset{\sim}{v}_h^* + \kappa \underset{\sim}{\overline{v}}_h$ with $\kappa = \frac{2C_1C_2}{(C_2)^2+2}$. By the Schwarz inequality, the elementary inequality, and (2.15)–(2.17), we obtain

$$\begin{aligned}
(\operatorname{div} \underset{\sim}{v}_h, q_h) &= (\operatorname{div} \underset{\sim}{v}_h^*, q_h^*) + \kappa(\operatorname{div} \underset{\sim}{\overline{v}}_h, \overline{q}_h) + \kappa(\operatorname{div} \underset{\sim}{\overline{v}}_h, q_h^*),\\
&\geqslant C_1 \|q_h^*, \|_{0,\Omega}^2 + C_2\kappa \|\overline{q}_h\|_{0,\Omega}^2 + \kappa(\operatorname{div} \underset{\sim}{\overline{v}}_h, q_h^*),\\
&\geqslant C_1 \|q_h^*\|_{0,\Omega}^2 + C_2\kappa \|\overline{q}_h\|_{0,\Omega}^2 - \sqrt{2}\kappa \left(\frac{C_2}{2\sqrt{2}} |\underset{\sim}{\overline{v}}_h|_{1,h}^2 + \frac{\sqrt{2}}{2C_2} \|q_h^*\|_{0,\Omega}^2 \right),\\
&= \left(C_1 - \frac{\kappa}{C_2} \right) \|q_h^*\|_{0,\Omega}^2 + \frac{C_2\kappa}{2} \|\overline{q}_h\|_{0,\Omega}^2 = \frac{C_1 (C_2)^2}{(C_2)^2+2} \|q_h\|_{0,\Omega}^2.
\end{aligned}$$

From $|\underset{\sim}{v}_h^*|_{1,h} = \|q_h^*\|_{0,\Omega}$, $|\underset{\sim}{\overline{v}}_h|_{1,h} = \|\overline{q}_h\|_{0,\Omega}$, and the Poincaré inequality, we have $\|\underset{\sim}{v}_h\|_{1,h} \lesssim \|q_h\|_{0,\Omega}$. This completes the proof of (2.7) and the proof of Theorem 2.2. ∎

2.3. **Proof of the discrete Korn's inequality**

For the discrete Korn's inequality, we follow the lines of [29]. We first introduce an auxiliary element scheme constructed by adding element bubble functions to the standard Bernardi–Raugel element [5]. We denote

$$\underset{\sim}{P}_T := \big(P_1(T)\big)^2 \oplus \operatorname{span}\{\lambda_2\lambda_3\mathbf{n}_1,\ \lambda_3\lambda_1\mathbf{n}_2, \lambda_1\lambda_2\mathbf{n}_3\} \oplus \big(\operatorname{span}\{\lambda_1\lambda_2\lambda_3\}\big)^2.$$

Define

$$\underset{\sim}{C}_h := \left\{ \underset{\sim}{z}_h \in \underset{\sim}{H}^1(\Omega) : \begin{array}{r} \underset{\sim}{z}_h|_T \in \underset{\sim}{P}_T, \forall\, T \in \mathcal{T}_h,\ \underset{\sim}{z}_h(a) \text{ is continuous at any } a \in \mathcal{N}_h^i, \\ \text{and } \fint_e \underset{\sim}{z}_h \cdot \mathbf{n}_e \,\mathrm{d}s \text{ is continuos across any } e \in \mathcal{E}_h^i \end{array} \right\},$$

and $\underset{\sim}{C}_h^N := \{\underset{\sim}{z}_h \in \underset{\sim}{C}_h :\ \underset{\sim}{z}_h(a) = \underset{\sim}{0},\ \forall\, a \in \Gamma_N \text{ and } \fint_e \underset{\sim}{z}_h \cdot \mathbf{n}_e \,\mathrm{d}s = 0,\ \forall\, e \subset \Gamma_N\}$, where $\Gamma_N = \partial\Omega\backslash\Gamma_D$. Here, we are concerned about the case of $\Gamma_D \neq \partial\Omega$, in which the discrete Korn's inequality plays a crucial role for outflow conditions.

2.3.1. *Technical lemmas*

Lemma 2.10. *The element pair $\underset{\sim}{C}_h^N \times Q_h$ satisfies the inf-sup condition*

$$\sup_{\underset{\sim}{z}_h \in \underset{\sim}{C}_h^N} \frac{\int_\Omega \operatorname{div} \underset{\sim}{z}_h\, q_h \,\mathrm{d}\Omega}{|\underset{\sim}{z}_h|_{1,h}} \gtrsim \|q_h\|_{0,\Omega}, \quad \forall\, q_h \in Q_h. \tag{2.18}$$

Proof. Let $\underset{\sim}{H}_N^1(\Omega) := \{\underset{\sim}{v} \in \underset{\sim}{H}^1(\Omega) :\ \underset{\sim}{v} = 0 \text{ on } \Gamma_N\}$. Define $\Pi_C :\ \underset{\sim}{H}_N^1(\Omega) \mapsto \underset{\sim}{C}_h^N$ by

$$\begin{cases} \Pi_C\, \underset{\sim}{v}\,(a) = R_h\, \underset{\sim}{v}\,(a), \quad \forall\, a \in \mathcal{N}_h, \\ \displaystyle\int_e (\Pi_C\, \underset{\sim}{v} - \underset{\sim}{v}) \cdot \mathbf{n}_e \,\mathrm{d}s = 0, \quad \forall\, e \in \mathcal{E}_h, \\ \displaystyle\int_T x\ \operatorname{div}(\Pi_C\, \underset{\sim}{v} - \underset{\sim}{v}) \,\mathrm{d}T = 0, \quad \int_T y\ \operatorname{div}(\Pi_C\, \underset{\sim}{v} - \underset{\sim}{v}) \,\mathrm{d}T = 0, \quad \forall\, T \in \mathcal{T}_h, \end{cases}$$

where R_h represents the local L^2-projection given in [18, (A.53)–(A.54)]. It can be verified that $(\operatorname{div} \Pi_C\, \underset{\sim}{v}, q_h) = (\operatorname{div} \underset{\sim}{v}, q_h)$ for any $q_h \in Q_h$, $|\Pi_C\, \underset{\sim}{v}|_{1,h} \lesssim |\underset{\sim}{v}|_{1,h}$, and Π_C is a Fortin operator. Hence, the stability (2.18) is valid [16, Propositions 4.1–4.2]. ∎

Lemma 2.11. *For any $\underset{\sim}{v} \in \underset{\sim}{V}_{hD}$ and $\underset{\sim}{z} \in \underset{\sim}{C}_h^N$, it holds that*

$$\sum_{T \in \mathcal{T}_h} \int_T \nabla \underset{\sim}{v} : \operatorname{curl} \underset{\sim}{z} \,\mathrm{d}T = 0. \tag{2.19}$$

Proof. Let subscripts "$\cdot_1$" and "$\cdot_2$" represent the components of the vector in the x and y directions, respectively. Integration by parts and direct calculation lead to

$$\begin{aligned} \sum_{T \in \mathcal{T}_h} \int_T \nabla \underset{\sim}{v} : \operatorname{curl} \underset{\sim}{z} \,\mathrm{d}T &= \sum_{T \in \mathcal{T}_h} \sum_{e \subset \partial T} \int_e (v_1 \nabla z_1 \cdot \mathbf{t}_{T,e} + v_2 \nabla z_2 \cdot \mathbf{t}_{T,e}) \,\mathrm{d}s \\ &= \sum_{T \in \mathcal{T}_h} \sum_{e \subset \partial T} \int_e (\underset{\sim}{v} \cdot \mathbf{n}_{T,e})(\underset{\sim}{g}_{T,e} \cdot \mathbf{n}_{T,e}) + (\underset{\sim}{v} \cdot \mathbf{t}_{T,e})(\underset{\sim}{g}_{T,e} \cdot \mathbf{t}_{T,e}) \,\mathrm{d}s, \end{aligned} \tag{2.20}$$

where $\underset{\sim}{g}_{T,e} := \nabla \underset{\sim}{z} \cdot \mathbf{t}_{T,e}$, $\mathbf{t}_{T,e}$ is the counterclockwise unit tangent vector of T on e, and $\mathbf{n}_{T,e}$ represents the unit outer normal vector. Note that $\underset{\sim}{z}|_e \in (P_1)^2 + \operatorname{span}\{\phi_{T,e} \cdot \mathbf{n}_{T,e}\}$, and $\phi_{T,e}$ is the quadratic bubble function associated with e in T, so we derive that $\underset{\sim}{g}_{T,e} \cdot \mathbf{t}_{T,e}$ is constant on each $e \subset \partial T$. We check the right-hand side of (2.20) case by case.

Case 1. For $e \in \mathcal{E}_h^i$ with $T_1 \cap T_2 = e$. Utilizing the continuity of $\underset{\sim}{v} \cdot \mathbf{n}$, $\mathbf{n}_{T_1,e} = -\mathbf{n}_{T_2,e}$, $\mathbf{t}_{T_1,e} = -\mathbf{t}_{T_2,e}$, and $\underset{\sim}{g}_{T_1,e} = -\underset{\sim}{g}_{T_2,e}$ by $\underset{\sim}{z} \in \underset{\sim}{H}^1(\Omega)$, we obtain

$$\int_e (\underset{\sim}{v} \cdot \mathbf{n}_{e,T_1})(\underset{\sim}{g}_{T_1,e} \cdot \mathbf{n}_{e,T_1}) + \int_e (\underset{\sim}{v} \cdot \mathbf{n}_{T_2,e})(\underset{\sim}{g}_{T_2,e} \cdot \mathbf{n}_{T_2,e})\,\mathrm{d}s = \int_e \underset{\sim}{v} \cdot \mathbf{n}_{e,T_1}(\underset{\sim}{g}_{T_1,e} \cdot \mathbf{n}_{T_1,e} - \underset{\sim}{g}_{T_1,e} \cdot \mathbf{n}_{T_1,e})\,\mathrm{d}s = 0.$$

At the same time, utilizing the continuity of $\int_e \underset{\sim}{v} \cdot \mathbf{t}\,\mathrm{d}s$ across interior edges, and noticing that $\underset{\sim}{g}_{T_1,e} \cdot \mathbf{t}_{T_1,e} = \underset{\sim}{g}_{T_2,e} \cdot \mathbf{t}_{T_2,e} = c$, where c represents a constant on e, we have

$$\int_e (\underset{\sim}{v} \cdot \mathbf{t}_{T_1,e})(\underset{\sim}{g}_{T_1,e} \cdot \mathbf{t}_{T_1,e}) + \int_e (\underset{\sim}{v} \cdot \mathbf{t}_{T_2,e})(\underset{\sim}{g}_{T_2,e} \cdot \mathbf{t}_{T_2,e})\,\mathrm{d}s = (\underset{\sim}{g}_{T_1,e} \cdot \mathbf{t}_{T_1,e})\left(\int_e \underset{\sim}{v} \cdot \mathbf{t}_{T_1,e}\,\mathrm{d}s + \int_e \underset{\sim}{v} \cdot \mathbf{t}_{T_2,e}\,\mathrm{d}s\right)\mathrm{d}s = 0.$$

Case 2. For $e \subset \Gamma_D$, $\underset{\sim}{v} \cdot \mathbf{n}_e = \int_e \underset{\sim}{v} \cdot \mathbf{t}_e\,\mathrm{d}s = 0$, and $\underset{\sim}{g}_{T,e} \cdot \mathbf{t}_e$ is constant on $e \subset T$. Therefore,

$$\int_e (\underset{\sim}{v} \cdot \mathbf{n}_{T,e})(\underset{\sim}{g}_{T,e} \cdot \mathbf{n}_{T,e}) + (\underset{\sim}{v} \cdot \mathbf{t}_{T,e})(\underset{\sim}{g}_{T,e} \cdot \mathbf{t}_{T,e})\,\mathrm{d}s = 0, \quad \forall\, e \subset \Gamma_D.$$

Case 3. For $e \subset \Gamma_N$, we have $\underset{\sim}{z}|_e = \underset{\sim}{0}$ by definition. Hence, $\underset{\sim}{g}_{T,e} = \underset{\sim}{0}$ for $e \subset T$, and

$$\int_e (\underset{\sim}{v} \cdot \mathbf{n}_{T,e})(\underset{\sim}{g}_{T,e} \cdot \mathbf{n}_{T,e}) + (\underset{\sim}{v} \cdot \mathbf{t}_{T,e})(\underset{\sim}{g}_{T,e} \cdot \mathbf{t}_{T,e})\,\mathrm{d}s = 0, \quad \forall\, e \subset \Gamma_N.$$

Namely, the right-hand-side of (2.20) equals zero. The proof is completed. ∎

2.3.2. *Proof of Theorem 2.3*

Proof of Theorem 2.3. For any $\underset{\sim}{v} \in \underset{\sim}{V}_{hD}$, $\epsilon(\underset{\sim}{v})|_T = (\nabla \underset{\sim}{v} - \frac{1}{2}\,\mathrm{rot}\ \underset{\sim}{v}\,\chi)|_T$, where $\chi = \left(\begin{smallmatrix} 0 & -1 \\ 1 & 0 \end{smallmatrix}\right)$. From (2.18) and $\mathrm{rot}\ \underset{\sim}{v} \in Q_h$, there exists some $\underset{\sim}{z} \in \underset{\sim}{C}_h^N$ such that

$$\int_\Omega \mathrm{div}\,\underset{\sim}{z}\, q\,\mathrm{d}\Omega = \sum_{T \in \mathcal{T}_h} \int_T \mathrm{rot}\ \underset{\sim}{v}\, q\,\mathrm{d}T, \quad \forall\, q \in Q_h \quad \text{and} \quad |\underset{\sim}{z}|_{1,h} \lesssim \|\,\mathrm{rot}\ \underset{\sim}{v}\|_{0,\Omega} \lesssim |\underset{\sim}{v}|_{1,h}.$$

Therefore, $\|\nabla \underset{\sim}{v} - \mathrm{curl}\ \underset{\sim}{z}\|_{0,\Omega} \leqslant |\underset{\sim}{v}|_{1,h} + |\underset{\sim}{z}|_{1,h} \lesssim |v|_{1,h}$, and

$$\begin{aligned}
\sum_{T \in \mathcal{T}_h} \int_T \epsilon(\underset{\sim}{v}) : (\nabla \underset{\sim}{v} - \mathrm{curl}\ \underset{\sim}{z})\,\mathrm{d}T &= \sum_{T \in \mathcal{T}_h} \int_T (\nabla \underset{\sim}{v} - \frac{1}{2}\,\mathrm{rot}\ \underset{\sim}{v}\,\chi) : (\nabla \underset{\sim}{v} - \mathrm{curl}\ \underset{\sim}{z})\,\mathrm{d}T \\
&= \sum_{T \in \mathcal{T}_h} \int_T |\nabla \underset{\sim}{v}|^2\,\mathrm{d}T - \frac{1}{2} \sum_{T \in \mathcal{T}_h} \int_T \mathrm{rot}\ \underset{\sim}{v}\,(\mathrm{rot}\ \underset{\sim}{v} - \mathrm{div}\,\underset{\sim}{z})\,\mathrm{d}T \\
&= \sum_{T \in \mathcal{T}_h} \int_T |\nabla \underset{\sim}{v}|^2\,\mathrm{d}T = |\underset{\sim}{v}|_{1,h}^2.
\end{aligned}$$

Finally, we have $\left(\sum_{T \in \mathcal{T}_h} \int_T |\epsilon(\underset{\sim}{v})|^2\,\mathrm{d}T\right)^{\frac{1}{2}} \geqslant \frac{\sum_{T \in \mathcal{T}_h} \int_T \epsilon(\underset{\sim}{v}) : (\nabla \underset{\sim}{v} - \mathrm{curl}\ \underset{\sim}{z})\,\mathrm{d}T}{\|\nabla \underset{\sim}{v} - \mathrm{curl}\ \underset{\sim}{z}\|_{0,\Omega}} \gtrsim |v|_{1,h}$, and the proof is completed. ∎

3. Application to conservative flows

3.1. Application to the Stokes equations

Consider the stationary Stokes system:

$$\begin{cases} -\varepsilon^2 \Delta\, \underset{\sim}{u} + \nabla\, p = \underset{\sim}{f} & \text{in } \Omega, \\ \mathrm{div}\,\underset{\sim}{u} = g & \text{in } \Omega, \\ \underset{\sim}{u} = 0, & \text{on } \Gamma_D. \end{cases} \tag{3.1}$$

For simplicity of presentation, we only consider the case of $\partial\Omega = \Gamma_D$ herein. Extensions to other boundary conditions follow directly.

The discretization scheme of (3.1) reads: Find $(\underset{\sim}{u}_h, p_h) \in \underset{\sim}{V}_{h0} \times Q_{h*}$ such that

$$\begin{cases} \varepsilon^2(\nabla_h \underset{\sim}{u}_h, \nabla_h \underset{\sim}{v}_h) - (\operatorname{div} \underset{\sim}{v}_h, p_h) = \langle \underset{\sim}{f}, \underset{\sim}{v}_h \rangle & \forall\ \underset{\sim}{v}_h \in \underset{\sim}{V}_h, \\ (\operatorname{div} \underset{\sim}{u}_h, q_h) = \langle g, q_h \rangle & \forall\ q_h \in Q_h. \end{cases} \tag{3.2}$$

Based on the discussions in Section 2, Brezzi's conditions can be easily verified, and (3.2) is uniformly well-posed with respect to ε and h.

Theorem 3.1. *Let $(\underset{\sim}{u}, p)$ and $(\underset{\sim}{u}_h, p_h)$ be the solutions of* (3.1) *and* (3.2)*, respectively. The following estimates hold with $0 < r \leqslant 2$:*

$$|\underset{\sim}{u} - \underset{\sim}{u}_h|_{1,h} \lesssim h^r |\underset{\sim}{u}|_{r+1,\Omega} + h|\underset{\sim}{u}|_{2,\Omega},$$
$$\|p - p_h\|_{0,\Omega} \lesssim h^r |p|_{r,\Omega} + \varepsilon^2 (h^r |\underset{\sim}{u}|_{r+1,\Omega} + h|\underset{\sim}{u}|_{2,\Omega}).$$

Proof. As the mixed element is inf-sup stable and divergence-free, and $\underset{\sim}{v}_h \cdot \mathbf{n}$ is continuous, the following estimates are standard [7, 9, 13]:

$$|\underset{\sim}{u} - \underset{\sim}{u}_h|_{1,h} \lesssim \inf_{\underset{\sim}{w}_h \in \underset{\sim}{V}_h} |\underset{\sim}{u} - \underset{\sim}{w}_h|_{1,h} + \sup_{\underset{\sim}{v}_h \in \underset{\sim}{Z}_h(0)} \frac{\left|\sum_{e\in\mathcal{E}_h} \varepsilon^2 \int_e (\nabla \underset{\sim}{u} \cdot \mathbf{n}_e) \cdot [\![\underset{\sim}{v}_h]\!]\, \mathrm{d}s\right|}{\varepsilon^2 |\underset{\sim}{v}_h|_{1,h}},$$

$$\|p - p_h\|_{0,\Omega} \lesssim \varepsilon^2 |\underset{\sim}{u} - \underset{\sim}{u}_h|_{1,h} + \inf_{q_h \in Q_h} \|p - q_h\|_{0,\Omega} + \sup_{\underset{\sim}{v}_h \in \underset{\sim}{V}_h} \frac{\left|\sum_{e\in\mathcal{E}_h} \varepsilon^2 \int_e (\nabla \underset{\sim}{u} \cdot \mathbf{n}_e) \cdot [\![\underset{\sim}{v}_h]\!]\, \mathrm{d}s\right|}{|\underset{\sim}{v}_h|_{1,h}}.$$

The term $\inf_{\underset{\sim}{w}_h \in \underset{\sim}{V}_h} |\underset{\sim}{u} - \underset{\sim}{w}_h|_{1,h}$ is bounded by the interpolation error. As $\int_e \underset{\sim}{v}_h \,\mathrm{d}s$ is continuous across interior edges and vanishes on $\partial\Omega$, a standard estimate similar to that of the Crouzeix and Raviart element [12, Lemma 3] leads to

$$\left|\sum_{e\in\mathcal{E}_h} \varepsilon^2 \int_e (\nabla \underset{\sim}{u} \cdot \mathbf{n}_e) \cdot [\![\underset{\sim}{v}_h]\!]\, \mathrm{d}s\right| \lesssim \varepsilon^2 h |\underset{\sim}{u}|_{2,\Omega} |\underset{\sim}{v}_h|_{1,h}. \tag{3.3}$$

Hence, we derive

$$|\underset{\sim}{u} - \underset{\sim}{u}_h|_{1,h} \lesssim h^r |\underset{\sim}{u}|_{r+1,\Omega} + h|\underset{\sim}{u}|_{2,\Omega} \quad \text{with} \quad 0 < r \leqslant 2.$$

The above estimates together with $\inf_{q_h \in Q_h} \|p - q_h\|_{0,\Omega} \lesssim h^r |p|_{r,\Omega}$ lead to

$$\|p - p_h\|_{0,\Omega} \lesssim h^r |p|_{r,\Omega} + \varepsilon^2 (h^r |\underset{\sim}{u}|_{r+1,\Omega} + h|\underset{\sim}{u}|_{2,\Omega}) \quad \text{with} \quad 0 < r \leqslant 2.$$

The proof is completed. ∎

3.2. **Application to the Darcy–Stokes–Brinkman equations**

Consider the Darcy–Stokes–Brinkman equations:

$$\begin{cases} -\varepsilon^2 \Delta \underset{\sim}{u} + \underset{\sim}{u} + \nabla p = \underset{\sim}{f} & \text{in } \Omega, \\ \operatorname{div} \underset{\sim}{u} = g & \text{in } \Omega, \\ \underset{\sim}{u} \cdot \mathbf{n} = 0,\ \varepsilon\, \underset{\sim}{u} \cdot \mathbf{t} = 0 & \text{on } \partial\Omega, \end{cases} \tag{3.4}$$

where $\varepsilon \in (0, 1]$ is a parameter. When ε is not too small, and $g = 0$, it is a Stokes problem with an additional lower-order term. When $\varepsilon = 0$, the first equation becomes Darcy's law for porous medium flow. Most classic mixed elements fail to converge uniformly with respect to ε when applied to (3.4) [32].

The discretization scheme of (3.4) reads: Find $(\underset{\sim}{u}_h, p_h) \in \underset{\sim}{V}_{h0} \times Q_{h*}$ such that

$$\begin{cases} \varepsilon^2(\nabla_h \underset{\sim}{u}_h, \nabla_h \underset{\sim}{v}_h) + (\underset{\sim}{u}_h, \underset{\sim}{v}_h) - (\operatorname{div} \underset{\sim}{v}_h, p_h) = \langle \underset{\sim}{f}, \underset{\sim}{v}_h \rangle & \forall\ \underset{\sim}{v}_h \in \underset{\sim}{V}_h, \\ (\operatorname{div} \underset{\sim}{u}_h, q_h) = \langle g, q_h \rangle & \forall\ q_h \in Q_h. \end{cases} \tag{3.5}$$

As the finite element pair is stable and conservative, Brezzi's conditions can be easily verified for (3.5), and it is uniformly well-posed with respect to ε and h, provided $\int_\Omega g \,\mathrm{d}\Omega = 0$. Robust

convergence can be obtained both for smooth continuous solutions and for the case when the effect of the ε-dependent boundary layers is taken into account later.

Theorem 3.2. *If $\underset{\sim}{u} \in \underset{\sim}{H}^{r+1}(\Omega) \cap \underset{\sim}{H}_0^1(\Omega)$ and $p \in H^r(\Omega) \cap L_0^2(\Omega)$ with $0 < r \leqslant 2$, then*

$$\|\operatorname{div} \underset{\sim}{u} - \operatorname{div} \underset{\sim}{u}_h\|_{0,\Omega} \lesssim h^r |\underset{\sim}{u}|_{r+1,\Omega}, \tag{3.6}$$

$$\|\underset{\sim}{u} - \underset{\sim}{u}_h\|_{0,\Omega} + \varepsilon |\underset{\sim}{u} - \underset{\sim}{u}_h|_{1,h} \lesssim h^r(\varepsilon + h)|\underset{\sim}{u}|_{r+1,\Omega} + \varepsilon h |\underset{\sim}{u}|_{2,\Omega}, \tag{3.7}$$

$$\|p - p_h\|_{0,\Omega} \lesssim h^r |p|_{r,\Omega} + h^r(\varepsilon + h)|\underset{\sim}{u}|_{r+1,\Omega} + \varepsilon h |\underset{\sim}{u}|_{2,\Omega}. \tag{3.8}$$

Proof. Evidently, $\operatorname{div} \underset{\sim}{u}_h = \mathrm{P}_{Q_{h*}}(\operatorname{div} \underset{\sim}{u})$, where $\mathrm{P}_{Q_{h*}}$ represents the L^2-projection into Q_{h*}. Therefore, the first inequality, (3.6), follows from the estimation of the L^2-projection. For this conservative pair, the following estimates are standard (see, e.g., [9] and [32]),

$$\begin{aligned} &\|\underset{\sim}{u} - \underset{\sim}{u}_h\|_{0,\Omega} + \varepsilon |\underset{\sim}{u} - \underset{\sim}{u}_h|_{1,h} \\ &\qquad \lesssim \inf_{\underset{\sim}{w}_h \in \underset{\sim}{V}_h} (\|\underset{\sim}{u} - \underset{\sim}{w}_h\|_{0,\Omega} + \varepsilon |\underset{\sim}{u} - \underset{\sim}{w}_h|_{1,h}) + \sup_{\underset{\sim}{v}_h \in \underset{\sim}{Z}_h(0)} \frac{\left|\sum_{e \in \mathcal{E}_h} \varepsilon^2 \int_e (\nabla \underset{\sim}{u} \cdot \mathbf{n}_e) \cdot [\![\underset{\sim}{v}_h]\!] \,\mathrm{d}s\right|}{\varepsilon |\underset{\sim}{v}_h|_{1,h}}, \end{aligned} \tag{3.9}$$

$$\begin{aligned} \|p - p_h\|_{0,\Omega} &\lesssim \|\underset{\sim}{u} - \underset{\sim}{u}_h\|_{0,\Omega} + \varepsilon |\underset{\sim}{u} - \underset{\sim}{u}_h|_{1,h} \\ &\quad + \inf_{q_h \in Q_h} \|p - q_h\|_{0,\Omega} + \sup_{\underset{\sim}{v}_h \in \underset{\sim}{V}_h} \frac{\left|\sum_{e \in \mathcal{E}_h} \varepsilon^2 \int_e (\nabla \underset{\sim}{u} \cdot \mathbf{n}_e) \cdot [\![\underset{\sim}{v}_h]\!] \,\mathrm{d}s\right|}{\varepsilon |\underset{\sim}{v}_h|_{1,h}}. \end{aligned} \tag{3.10}$$

Hence, (3.7) and (3.8) are derived in a similar way as those in Theorem 3.1. ∎

As is mentioned in [32], it may happen that $|\underset{\sim}{u}|_{2,\Omega}$ and $|\underset{\sim}{u}|_{3,\Omega}$ blow up as ε tends to 0. In this case, the convergence estimates given in Theorem 3.2 will deteriorate, especially when the solution of (3.4) has boundary layers. To derive a uniform convergence analysis of the discrete solutions, we assume that Ω is a convex polygon. Let $\{a_j := (x_j, y_j)\}$ denote the set of corner nodes of Ω. Define

$$H_+^1(\Omega) := \left\{ g \in H^1(\Omega) \cap L_0^2(\Omega) : \ \int_\Omega \frac{|g(x,y)|}{(x - x_j)^2 + (y - y_j)^2} \,\mathrm{d}\Omega < \infty, \ j = 1, 2, \ldots, l \right\},$$

with associated norm

$$\|g\|_{1,+}^2 := \|g\|_{1,\Omega}^2 + \sum_{j=1}^{l} \int_\Omega \frac{|g(x,y)|}{(x - x_j)^2 + (y - y_j)^2} \,\mathrm{d}\Omega.$$

Let $(\underset{\sim}{u}^0, p^0)$ solve (3.4) in the case of $\varepsilon = 0$. Then, it is proved in [32] that

$$\varepsilon^2 \|\underset{\sim}{u}\|_{2,\Omega} + \varepsilon \|\underset{\sim}{u}\|_{1,\Omega} + \|\underset{\sim}{u} - \underset{\sim}{u}^0\|_{0,\Omega} + \|p - p^0\|_{1,\Omega} + \varepsilon^{\frac{1}{2}} \|\underset{\sim}{u}^0\|_{1,\Omega} + \varepsilon^{\frac{1}{2}} \|p^0\|_{1,\Omega} \lesssim \varepsilon^{\frac{1}{2}} (\|\underset{\sim}{f}\|_{\mathrm{rot}} + \|g\|_{1,+}), \tag{3.11}$$

where $\|\cdot\|_{\mathrm{rot}} := \|\cdot\|_{0,\Omega} + \|\operatorname{rot}(\cdot)\|_{0,\Omega}$ is the norm defined in $\underset{\sim}{H}(\mathrm{rot}, \Omega)$. Following the technique in [32], we can obtain the following uniform convergence estimate.

Theorem 3.3. *Let $(\underset{\sim}{u}, p)$ be the exact solution of (3.4) and $(\underset{\sim}{u}_h, p_h)$ be its approximation in $\underset{\sim}{V}_{h0} \times Q_{h*}$. If $\underset{\sim}{f} \in \underset{\sim}{H}(\mathrm{rot}, \Omega)$ and $g \in H_+^1(\Omega)$, then*

$$\|\operatorname{div} \underset{\sim}{u} - \operatorname{div} \underset{\sim}{u}_h\| \lesssim h \|g\|_{1,\Omega}, \tag{3.12}$$

$$\|\underset{\sim}{u} - \underset{\sim}{u}_h\|_{0,\Omega} + \varepsilon |\underset{\sim}{u} - \underset{\sim}{u}_h|_{1,h} \lesssim h^{\frac{1}{2}} (\|\underset{\sim}{f}\|_{\mathrm{rot}} + \|g\|_{1,+}), \tag{3.13}$$

$$\|p - p_h\|_{0,\Omega} \lesssim h^{\frac{1}{2}} (\|\underset{\sim}{f}\|_{\mathrm{rot}} + \|g\|_{1,+}). \tag{3.14}$$

Proof. The first estimate is direct , $as\, \mathrm{div}\, \underset{\sim}{u} = g$. To obtain the second inequality, we first analyze the interpolation error. By (2.5), (2.6), and (3.11), we have

$$\begin{aligned}\|\underset{\sim}{u} - \Pi_h \underset{\sim}{u}\|_{0,\Omega} &\leqslant \|(\mathrm{I} - \Pi_h)(\underset{\sim}{u} - \underset{\sim}{u}^0\|_{0,\Omega} + \|\underset{\sim}{u}^0 - \Pi_h \underset{\sim}{u}^0\|_{0,\Omega}, \\ &\lesssim h^{\frac{1}{2}}(\|\underset{\sim}{u} - \underset{\sim}{u}^0\|_{0,\Omega}^{\frac{1}{2}} \|\underset{\sim}{u} - \underset{\sim}{u}^0\|_{1,\Omega}^{\frac{1}{2}} + h^{\frac{1}{2}} \|\underset{\sim}{u}^0\|_{1,\Omega}) \lesssim h^{\frac{1}{2}}(\|\underset{\sim}{f}\|_{\mathrm{rot}} + \|g\|_{1,+}).\end{aligned} \tag{3.15}$$

At the same time,

$$\varepsilon |\underset{\sim}{u} - \Pi_h \underset{\sim}{u}|_{1,h} \lesssim \varepsilon |\underset{\sim}{u}|_{1,\Omega}^{\frac{1}{2}} |\underset{\sim}{u} - \Pi_h \underset{\sim}{u}|_{1,h}^{\frac{1}{2}} \lesssim \varepsilon h^{\frac{1}{2}} |\underset{\sim}{u}|_{1,\Omega}^{\frac{1}{2}} |\underset{\sim}{u}|_{2,\Omega}^{\frac{1}{2}} \lesssim h^{\frac{1}{2}}(\|\underset{\sim}{f}\|_{\mathrm{rot}} + \|g\|_{1,+}), \tag{3.16}$$

where we utilize $\varepsilon |\underset{\sim}{u}|_{1,\Omega}^{\frac{1}{2}} |\underset{\sim}{u}|_{2,\Omega}^{\frac{1}{2}} \lesssim \varepsilon^{\frac{1}{2}} |\underset{\sim}{u}|_{1,\Omega} + \varepsilon^{\frac{3}{2}} |\underset{\sim}{u}|_{2,\Omega} \lesssim \|\underset{\sim}{f}\|_{\mathrm{rot}} + \|g\|_{1,+}$.
By the continuity of $\underset{\sim}{v}_h \cdot \mathbf{n}_e$ and $\int_e \underset{\sim}{v}_h \cdot \mathbf{t}_e \,\mathrm{d}s$, a standard estimate (see, e.g., [32, Lemma 5.1]) yields $\sum_{e\in\mathcal{E}_h} \varepsilon^2 \int_e (\nabla \underset{\sim}{u} \cdot \mathbf{n}_e) \cdot [\![\underset{\sim}{v}_h]\!] \,\mathrm{d}s \lesssim \varepsilon^2 h^{\frac{1}{2}} |\underset{\sim}{u}|_{1,\Omega}^{\frac{1}{2}} |\underset{\sim}{u}|_{2,\Omega}^{\frac{1}{2}} |\underset{\sim}{v}_h|_{1,h}$. Then, we derive

$$\frac{\left|\sum_{e\in\mathcal{E}_h} \varepsilon^2 \int_e (\nabla \underset{\sim}{u} \cdot \mathbf{n}_e) \cdot [\![\underset{\sim}{v}_h]\!] \,\mathrm{d}s\right|}{\varepsilon |\underset{\sim}{v}_h|_{1,h}} \lesssim \varepsilon h^{\frac{1}{2}} |\underset{\sim}{u}|_{1,\Omega}^{\frac{1}{2}} |\underset{\sim}{u}|_{2,\Omega}^{\frac{1}{2}} \lesssim h^{\frac{1}{2}}(\|\underset{\sim}{f}\|_{\mathrm{rot}} + \|g\|_{1,+}). \tag{3.17}$$

A combination of(3.9), (3.15), (3.16), and (3.17) leads to

$$\|\underset{\sim}{u} - \underset{\sim}{u}_h\|_{0,\Omega} + \varepsilon |\underset{\sim}{u} - \underset{\sim}{u}_h|_{1,h} \lesssim h^{\frac{1}{2}}(\|\underset{\sim}{f}\|_{\mathrm{rot}} + \|g\|_{1,+}). \tag{3.18}$$

Again from (3.11), note that $\varepsilon < 1$, so we have

$$\|p - \Pi_{Q_{h*}} p\|_{0,\Omega} \lesssim h|p|_{1,\Omega} \lesssim h|p - p^0|_{1,\Omega} + h|p^0|_{1,\Omega} \lesssim h(\|\underset{\sim}{f}\|_{\mathrm{rot}} + \|g\|_{1,+}). \tag{3.19}$$

Hence, by (3.10), (3.18), and (3.19), the last estimate of (3.14) is derived. ∎

4. Numerical Experiments

In this section, we carry out numerical experiments to validate the theory and illustrate the capacity of the newly proposed element pair. Examples are given as illustrations from different perspectives.

- Examples 4.1 and 4.2 test the method with the Stokes problem, especially its robustness with respect to the Reynolds number and the triangulations;
- Examples 4.3 and 4.4 test the method with the Darcy–Stokes–Brinkman equation, especially the robustness with respect to the small parameter, for smooth solutions as well as solutions with sharp layers;
- Examples 4.5 and 4.6 test the method with the incompressible Navier–Stokes equation, regarding evolutionary and steady states.

Three kinds of $P_2 - P_1$ pairs are involved in the experiments, namely,

TH: the Taylor–Hood element pair with continuous vector P_2 functions for the velocity space and continuous P_1 functions for the pressure space;

SV: the Scott–Vogelius element pair with continuous vector P_2 functions for the velocity space and discontinuous P_1 functions for the pressure space;

NPP: the newly proposed $P_2 - P_1$ element pair.

All simulations are performed on uniformly refined grids. For the SV pair, an additional barycentric refinement is applied on each grid to guarantee the stability.

Example 4.1. This example was suggested in [27] to illustrate the non-pressure-robustness of classical elements. Let $\Omega = (0,1)^2$. Consider the Stokes equations in (3.1), with $\varepsilon^2 = 1$, $g = 0$, and $\underset{\sim}{f} = (0, Ra(1-y+3y^2))^T$, where $Ra > 0$ represents a parameter. No-slip boundary conditions are imposed on $\partial\Omega$. The exact solution pair is $\underset{\sim}{u} = \underset{\sim}{0}$ and $p = Ra(y^3 - \frac{y^2}{2} + y - \frac{7}{12})$.

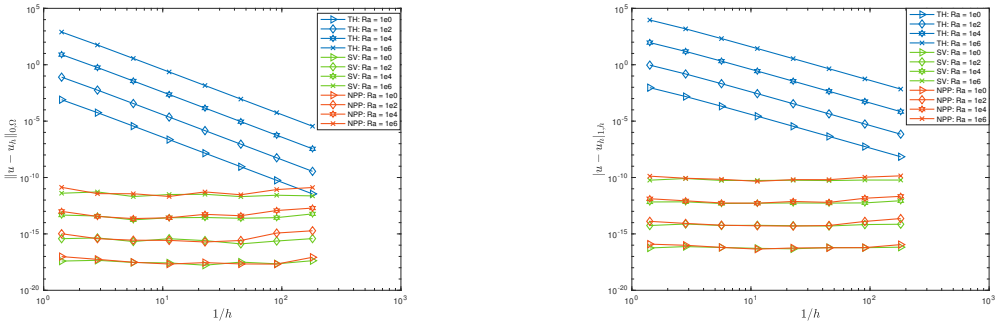

FIGURE 4.1. Example 4.1: Velocity errors in the no-flow Stokes equations by the TH, SV, and NPP pairs.

For the continuous problem, different values of Ra result in different exact pressures and the same exact velocity vector. As is shown in Figure 4.1, for both the SV and NPP pairs, the numerical velocities are close to zero for different values of Ra. However, for the TH pair, the discrete velocity is far from zero, even when $Ra = 1$. It demonstrates the advantage of pressure-robust pairs especially for problems with large pressures.

Example 4.2. This example was also introduced in [27]. Let $\Omega = (0,4)\times(0,2)\backslash[2,4]\times[0,1]$. Consider a flow with Coriolis forces with the following form

$$\begin{cases} -\varepsilon^2 \Delta \underset{\sim}{u} + \nabla p + 2\,\underset{\sim}{w} \times \underset{\sim}{u} = \underset{\sim}{f} & \text{in } \Omega, \\ \operatorname{div} \underset{\sim}{u} = 0 & \text{in } \Omega, \end{cases}$$

where $\underset{\sim}{w} = (0,0,w)^T$ is a constant angular velocity vector. Changing the magnitude, w, will change only the exact pressure, and not the true velocity solution. Dirichlet boundary conditions are imposed on $\partial\Omega$; see Figure 4.2 (left). The computed domain and initial unstructured grid are depicted in Figure 4.2. Simulations are performed with $\varepsilon^2 = 0.01$, while $w = 100$ or $w = 1000$.

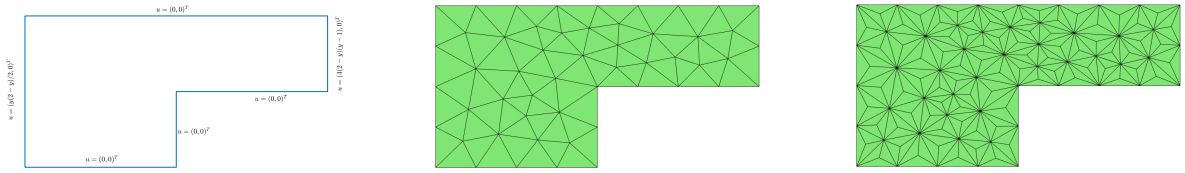

FIGURE 4.2. Example 4.2: Forward-facing step domain, unstructured mesh (level 1), and unstructured barycentric mesh for the SV pair (level 1).

Computed velocities (speed) with $w = 100$ and $w = 1000$ are depicted in Figures 4.3 and 4.4, respectively. The solutions computed with the SV and NPP pairs are considerably more accurate compared with the TH pair. Even on the third-level grid, the advantages of divergence-free elements are more obvious when $w = 1000$.

To compare the mesh dependence of these three pairs, we apply them on a structured mesh without additional barycentric refinement (Figure 4.5). This type of mesh is generally considered of good

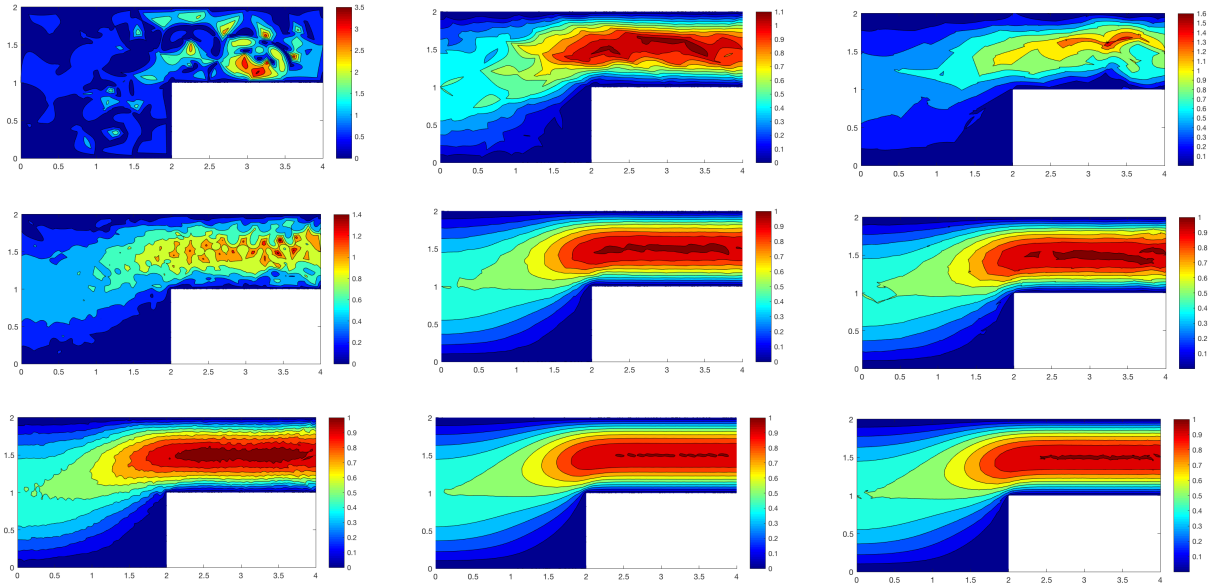

FIGURE 4.3. Example 4.2 ($w = 100$ and $\varepsilon^2 = 0.01$): Speed obtained by the TH pair (left column), the SV pair (middle column), and the NPP pair (right column); rows 1 – 3 are results on meshes 1– 3.

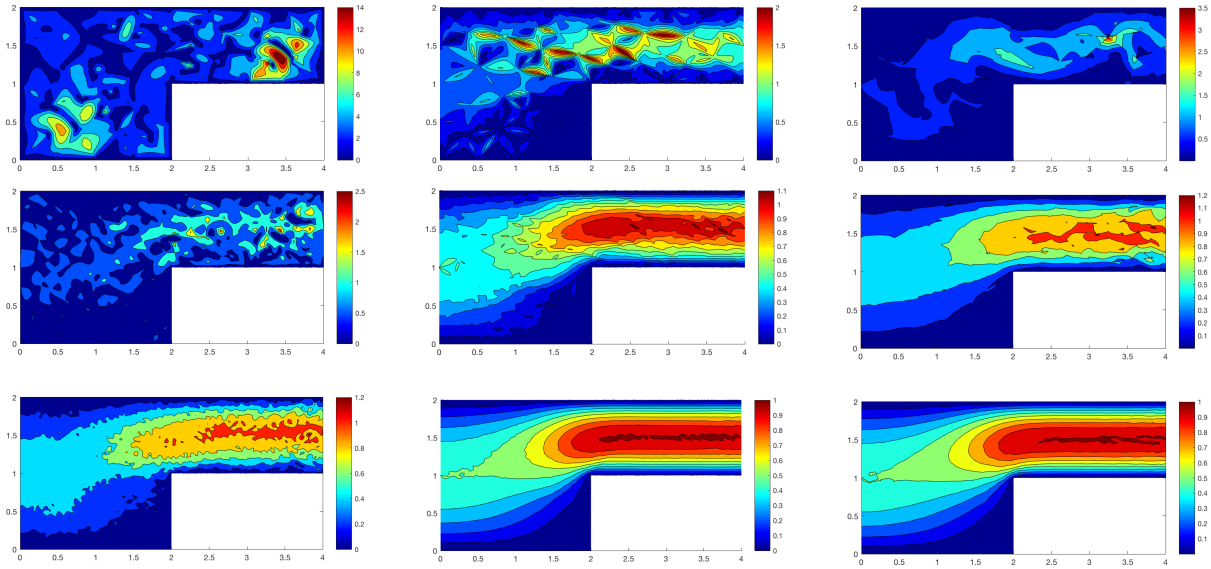

FIGURE 4.4. Example 4.2 ($w = 1000$ and $\varepsilon^2 = 0.01$): Speed obtained by the TH pair (left column), the SV (middle column), and the NPP pair (right column); rows 1 – 3 are results on meshes 1 – 3.

quality and commonly used. As is shown in Figure 4.6, the simulation by the SV pair turns out to be unreliable on the grid, while the NPP pair works fine.

FIGURE 4.5. Forward-facing step domain and structured non-barycentric mesh.

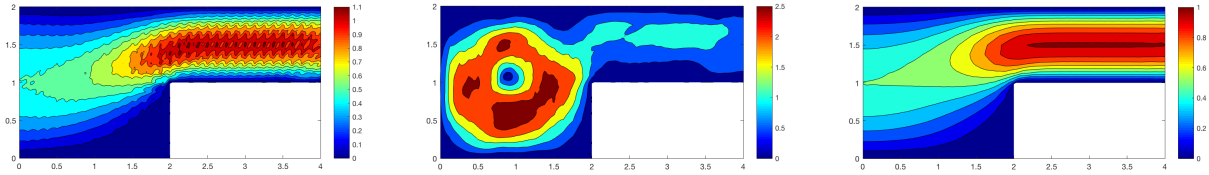

FIGURE 4.6. Example 4.2 ($w = 100$ and $\varepsilon^2 = 0.01$): Simulation by the SV pair (middle) is not as good as the TH pair (left) nor the NPP pair (right) on non-barycentric mesh.

Example 4.3. Let $\Omega = (0,1)^2$. We consider the Darcy–Stokes–Brinkman problem with

$$\underset{\sim}{u} = \operatorname{curl}\left(\sin^2(\pi x)\sin^2(\pi y)\right) = \pi \begin{pmatrix} \sin^2(\pi x)\sin(2\pi y) \\ -\sin^2(\pi y)\sin(2\pi x) \end{pmatrix}; \quad p = \frac{2}{\pi} - \sin(\pi x).$$

The force, $\underset{\sim}{f}$, is computed by $\underset{\sim}{f} = -\varepsilon^2\Delta\underset{\sim}{u} + \underset{\sim}{u} + \nabla p$, and $g = \operatorname{div}\underset{\sim}{u} = 0$. The solution is smooth and independent of ε. The initial triangulation is unstructured, and it is successively refined to maintain the quality of grids.

In Figure 4.7, we draw convergence curves of the NPP pair with different values of ε, where curves represent actual error declines, while triangles illustrate corresponding theoretical convergence rates. As is shown, when $0 < \varepsilon < 1$, errors in L^2-norm are of the $\mathcal{O}(h^2)$ order and errors in H^1-norm are of the $\mathcal{O}(h)$ order. In the limiting case of $\varepsilon = 0$, the L^2-norm error reaches the $\mathcal{O}(h^3)$ order and H^1-norm error reaches the $\mathcal{O}(h^2)$ order, which is because $\underset{\sim}{V}_{h0}$ is a conforming subspace of $\underset{\sim}{H}(\operatorname{div}\Omega)$.

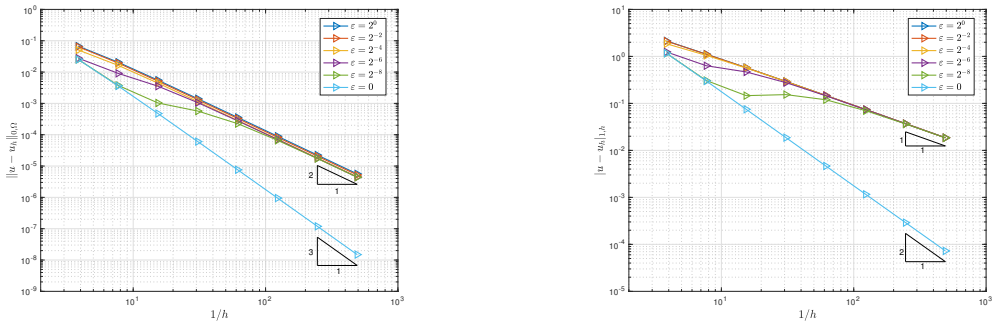

FIGURE 4.7. Example 4.3: Velocity errors in the L^2-norm (left) and in the H^1-norm (right) by the NPP method.

In Figure 4.8, we present the errors in the norm $|||\cdot|||_{\varepsilon,h}$ by the TH pair and the NPP pair when $\varepsilon = 2^{-8}$. Here, $|||\underset{\sim}{v}|||_{\varepsilon,h} := \varepsilon^2|\underset{\sim}{v}|^2_{1,h} + \|\underset{\sim}{v}\|_{0,\Omega} + \|\operatorname{div}\underset{\sim}{v}\|^2_{0,\Omega}$ is the commonly used norm, which combines the Stokes and Darcy problems. Although the convergence rate of the NPP pair is one order lower

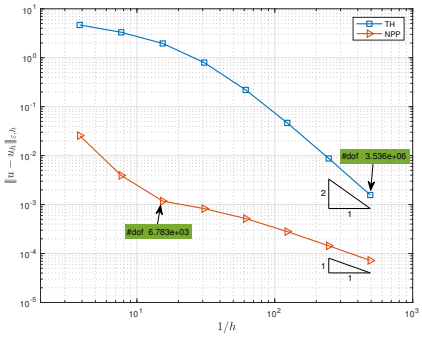

FIGURE 4.8. Example 4.3: Errors of velocity in the energy norm by the NPP pair and the TH pair when $\varepsilon = 2^{-8}$.

than that of the TH pair, the error of the former is smaller (several magnitudes) than that of the latter in the figure where millions of DOFs have been used on the finest grid. For the NPP pair, the associated energy error of velocity is close to 10^{-3}, while for the TH pair, it does not reach an error of 10^{-3} even on the eighth-level mesh. However, as shown in the figure, the degree of freedom of the TH pair (on the eighth-level mesh) is over 500 times more than the NPP pair (on the third-level mesh).

Example 4.4. Let $\Omega = (0,1)^2$. Consider the Darcy–Stokes–Brinkman problem with

$$\underset{\sim}{u} = \varepsilon \operatorname{curl}\left(e^{-\frac{xy}{\varepsilon}}\right) = \begin{pmatrix} -xe^{-\frac{xy}{\varepsilon}} \\ ye^{-\frac{xy}{\varepsilon}} \end{pmatrix}; \quad p = -\varepsilon e^{-\frac{x}{\varepsilon}}.$$

The boundary layers of the exact velocity, $\underset{\sim}{u}$, are shown in Figure 4.9.

FIGURE 4.9. Example 4.4: x-component (left) and y-component (right) of the exact velocity with boundary layers when $\varepsilon = 2^{-4}$.

From Table 4.1, the convergence rate of velocity is approximately one if ε is sufficiently large, and it decreases to half an order as ε approaches zero, which is consistent with the analysis in Theorem 3.3. From Table 4.2, the discrete pressure converges at $\mathcal{O}(h)$ order, which is higher than the theoretical estimation $\mathcal{O}(h^{1/2})$ order.

Example 4.5. Let $\Omega = (0,1)^2$. Consider the incompressible Navier–Stokes equations

$$\begin{cases} \partial_t \underset{\sim}{u} - \varepsilon^2 \Delta \underset{\sim}{u} + (\underset{\sim}{u} \cdot \nabla)\underset{\sim}{u} + \nabla p = \underset{\sim}{f} & \text{in } \Omega, \\ \operatorname{div} \underset{\sim}{u} = 0 & \text{in } \Omega, \end{cases} \tag{4.1}$$

with the prescribed solution

$$\underset{\sim}{u}(x,y,t) = \begin{pmatrix} \sin(1-x)\sin(y+t) \\ -\cos(1-x)\cos(y+t) \end{pmatrix}; \quad p = -\cos(1-x)\sin(y+t).$$

TABLE 4.1. Example 4.4 (with boundary layers): Errors of velocity in the energy norm by the NPP element.

$\varepsilon \setminus h$	2.599E-1	1.300E-01	6.498E-02	3.249E-02	1.625E-02	Rate
2^{-4}	2.998E-02	1.147E-02	4.958E-03	2.430E-03	1.228E-03	1.15
2^{-6}	6.589E-02	3.000E-02	1.159E-02	4.228E-03	1.753E-03	1.33
2^{-8}	1.061E-01	6.246E-02	3.238E-02	1.438E-02	5.504E-03	1.07
2^{-10}	1.171E-01	7.906E-02	5.147E-02	3.061E-02	1.601E-02	0.71
2^{-12}	1.234E-01	8.455E-02	5.688E-02	3.848E-02	2.529E-02	0.57

TABLE 4.2. Example 4.4 (with boundary layers): Errors of pressure in the L^2-norm by the NPP element.

$\varepsilon \setminus h$	2.599E-1	1.300E-01	6.498E-02	3.249E-02	1.625E-02	Rate
2^{-4}	2.260E-03	8.080E-04	2.884E-04	1.211E-04	5.702E-05	1.34
2^{-6}	2.779E-03	7.880E-04	2.696E-04	9.042E-05	2.938E-05	1.63
2^{-8}	6.283E-03	2.044E-03	5.366E-04	1.273E-04	3.448E-05	1.90
2^{-10}	6.730E-03	3.056E-03	1.339E-03	4.607E-04	1.235E-04	1.43
2^{-12}	6.710E-03	3.044E-03	1.440E-03	7.024E-04	3.216E-04	1.09

In this example, the Crank–Nicolson scheme is used for time discretization, and the Newton linearization is adopted to handle the nonlinear term. To isolate the spatial error, let the time-step $dt = 10^{-3}$ and the final time be 10^{-2}. The unstructured subdivisions illustrated in Example 4.2 are utilized.

As depicted in Table 4.3 with $\varepsilon^2 = 10^{-6}$, solutions by the TH pair converge with the $\mathcal{O}(h^{3/2})$ order in the L^2-norm, and by the SV pair, they converge with $\mathcal{O}(h^2)$ order. It was analyzed in [31] that the TH pair loses order mainly because it is not pressure-robust, while the suboptimal result of the SV pair is due to additional error sources arising from the nonlinear term. The NPP pair exhibits a convergence rate of $\mathcal{O}(h^2)$ order, which is consistent with its theoretical analysis, and it gives here an more accurate approximation than the SV pair.

TABLE 4.3. Example 4.5 ($\varepsilon^2 = 10^{-6}$): Errors of velocity in the L^2-norm.

	TH		SV		NPP	
h	$\|(\underset{\sim}{u} - \underset{\sim}{u}_h)(T)\|_{0,\Omega}$	Rate	$\|(\underset{\sim}{u} - \underset{\sim}{u}_h)(T)\|_{0,\Omega}$	Rate	$\|(\underset{\sim}{u} - \underset{\sim}{u}_h)(T)\|_{0,\Omega}$	Rate
2.599E-01	1.746E-04	–	1.031E-04	–	7.128E-05	–
1.300E-01	6.006E-05	1.54	1.362E-05	2.92	9.407E-06	2.92
6.498E-02	2.158E-05	1.48	1.989E-06	2.78	1.377E-06	2.77
3.249E-02	7.583E-06	1.51	3.561E-07	2.48	2.488E-07	2.47
1.625E-02	2.524E-06	1.59	7.790E-08	2.19	5.455E-08	2.19

Example 4.6. Let $\Omega = (0,1)^2$ be a square domain. Consider the Navier–Stokes equations in (4.1), with boundary conditions $\underset{\sim}{u} = (-1,0)^T$ on the side $y = 1$ and $\underset{\sim}{u} = (0,0)^T$ on the other three sides. Take $\varepsilon^2 = 10^{-3}$.

The backward-Euler time-stepping scheme and the Picard iteration are adopted for this example. Set the time step to be $dt = 0.1$. Consider a long time simulation with the final time of 90 to derive a steady solution. Indeed, as the solution is steady, the choice of time scheme has little influence on the accuracy of the final solution. Referenced data in a benchmark work [10] are involved to make

a reliable comparison, where the solutions are derived on a rather fine mesh, that is, a 1024×1024 rectangular subdivision of domain Ω. We want to see whether major features of the steady-state flow can be captured on a coarse mesh with $43 \times 43 \times 2$ cells.

Isolines of the streamfunction, vorticity, and pressure fields are displayed in Figures 4.10, 4.11, and 4.12, respectively. Compared with the TH pair, the shapes of contour maps derived by the NPP pair are closer to the reference solution. In particular, the colormap of pressure obtained by the NPP pair and the TH pair are quite different; note the difference between the sidebars. By the values given in [10, Table 1], the NPP pair method gives a more accurate approximation of pressure then the TH pair does.

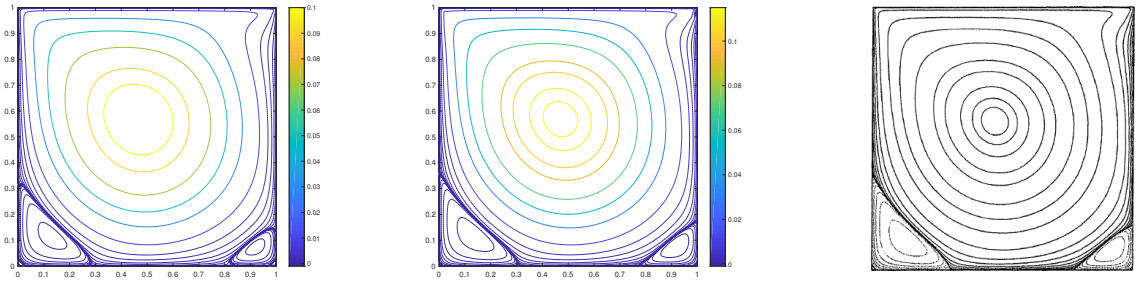

Figure 4.10. Example 4.6 (streamfunction): Isolines given by the NPP pair (middle) is closer to the reference solution in [10] (right) than the TH pair (left).

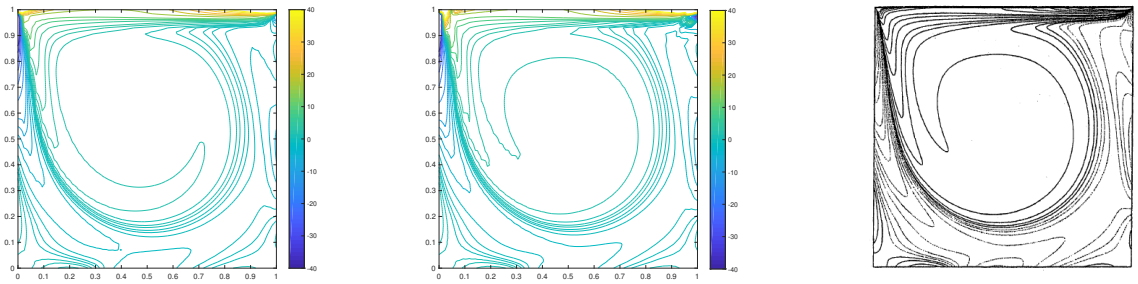

Figure 4.11. Example 4.6 (vorticity): Isolines derived by the NPP pair (middle) is closer to the reference solution in [10] (right) than the TH pair (left).

Figure 4.13 shows the velocity along the centerlines of the cavity. We can see that the results computed by the NPP pair are in better agreement with the reference results in [10] than the TH pair.

Moreover, the extremes of the streamfunction and the vorticity are depicted in Tables 4.4 and 4.5, respectively. Both of them indicate that the NPP pair gives closer results to the benchmark reference results.

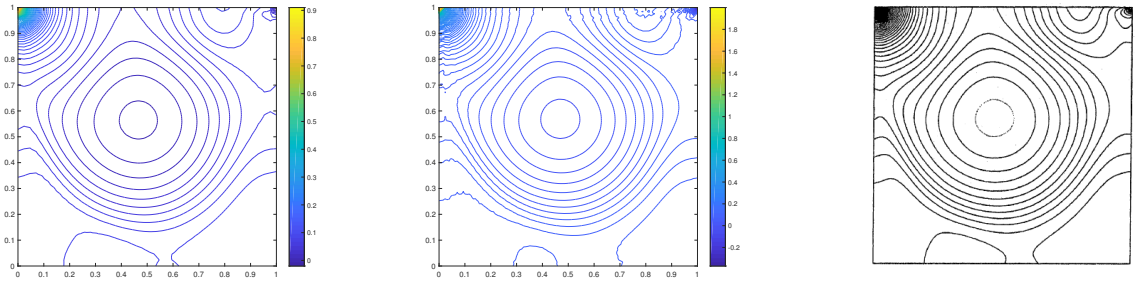

FIGURE 4.12. Example 4.6 (pressure): The extreme values of the pressure by the TH pair (left) is notably different from those by the NPP pair (middle), and the latter is closer to the reference values given in [10](right).

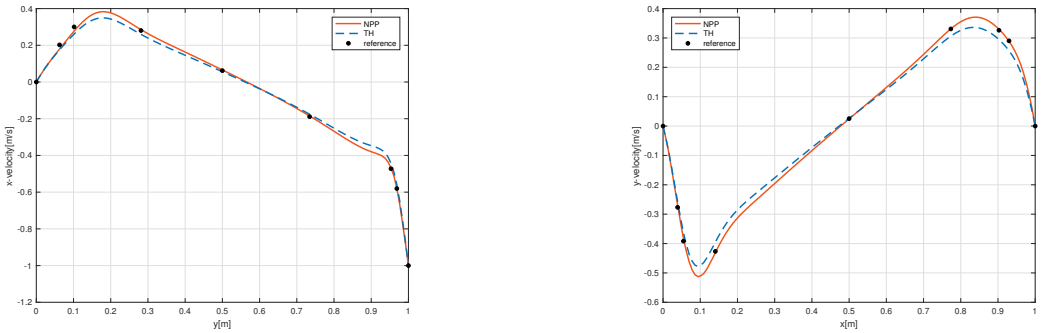

FIGURE 4.13. Example 4.6 (velocity profile): x-velocity through the vertical centerline $x = 0.5$ (left), and y-velocity through the horizontal centerline $y = 0.5$ (right).

TABLE 4.4. Example 4.6 (streamfunction): Values on the primary and the lower-left secondary vortices.

Scheme	Mesh	Primary	x	y	Secondary	x	y
TH	43×43	1.0862E-01	0.4688	0.5703	-1.3882E-03	0.1328	0.1094
NPP	43×43	1.1733E-01	0.4688	0.5703	-1.6221E-03	0.1406	0.1094
Ref.	1024×1024	1.1892E-01	0.4688	0.5654	-1.7292E-03	0.1367	0.1123

TABLE 4.5. Example 4.6 (vorticity): Values on the primary and the lower-left secondary vortices.

Scheme	Mesh	Primary	x	y	Secondary	x	y
TH	43×43	1.8976E+00	0.4688	0.5703	-9.1294E-01	0.1328	0.1094
NPP	43×43	2.0615E+00	0.4688	0.5703	-9.8718E-01	0.1406	0.1094
Ref.	1024×1024	2.0674E+00	0.4688	0.5654	-1.1120E+00	0.1367	0.1123

Acknowledgments

The authors would like to thank the anonymous referee for the valuable comments, which helped to improve the mathematical understanding and the presentation of the paper significantly.

References

[1] Douglas N. Arnold and Jinshui Qin. Quadratic velocity/linear pressure Stokes elements. In *Advances in Computer Methods for Partial Differential Equations VII*, pages 28–34. IMACS, 1992.

[2] Ferdinando Auricchio, Lourenço Beirão da Veiga, Carlo Lovadina, and Alessandro Reali. The importance of the exact satisfaction of the incompressibility constraint in nonlinear elasticity: mixed FEMs versus NURBS-based approximations. *Comput. Methods Appl. Mech. Eng.*, 199(5-8):314–323, 2010.

[3] Ferdinando Auricchio, Lourenço Beirão da Veiga, Carlo Lovadina, Alessandro Reali, Robert L. Taylor, and Peter Wriggers. Approximation of incompressible large deformation elastic problems: some unresolved issues. *Comput. Mech.*, 52(5):1153–1167, 2013.

[4] Blanca Ayuso De Dios, Franco Brezzi, Luisa D. Marini, Jinchao Xu, and Ludmil Zikatanov. A simple preconditioner for a discontinuous Galerkin method for the Stokes problem. *J. Sci. Comput.*, 58(3):517–547, 2014.

[5] Christine Bernardi and Geneviève Raugel. Analysis of some finite elements for the Stokes problem. *Math. Comput.*, 44:71–79, 1985.

[6] Susanne C. Brenner and Larkin R. Scott. *The mathematical theory of finite element methods*, volume 15 of *Texts in Applied Mathematics*. Springer, 2002.

[7] Franco Brezzi. On the existence, uniqueness and approximation of saddle-point problems arising from Lagrangian multipliers. *Rev. Franc. Automat. Inform. Rech. Operat.*, 8(R-2):129–151, 1974.

[8] Franco Brezzi, Jr Douglas, Jim, and Luisa D. Marini. Recent results on mixed finite element methods for second order elliptic problems. In *Vistas in applied mathematics*, pages 25–43. Optimization Software; Springer, 1986.

[9] Franco Brezzi and Michel Fortin. *Mixed and Hybrid Finite Element Methods*, volume 15 of *Springer Series in Computational Mathematics*. Springer, 1991.

[10] Charles-Henri Bruneau and Mazen Saad. The 2D lid-driven cavity problem revisited. *Comput. Fluids*, 35(3):326–348, 2006.

[11] Shaochun Chen, Lina Dong, and Zhonghua Qiao. Uniformly convergent $H(\mathrm{div})$-conforming rectangular elements for Darcy–Stokes problem. *Sci. China, Math.*, 56(12):2723–2736, 2013.

[12] Philippe G. Ciarlet. *The finite element method for elliptic problems*, volume 4 of *Studies in Mathematics and its Applications*. North-Holland, 1978.

[13] Michel Crouzeix and Pierre-Arnaud Raviart. Conforming and nonconforming finite element methods for solving the stationary Stokes equations. I. *Rev. Franc. Automat. Inform. Rech. Operat.*, 7(R-3):33–75, 1973.

[14] F. A. Dahlen. On the static deformation of an earth model with a fluid core. *Geophys. J. R. Astron. Soc.*, 36(2):461–485, 1974.

[15] Richard S. Falk and Michael Neilan. Stokes complexes and the construction of stable finite elements with pointwise mass conservation. *SIAM J. Numer. Anal.*, 51(2):1308–1326, 2013.

[16] Michel Fortin. An analysis of the convergence of mixed finite element methods. *RAIRO, Anal. Numér.*, 11(4):341–354, 1977.

[17] Nicolas R. Gauger, Alexander Linke, and Philipp W. Schroeder. On high-order pressure-robust space discretisations, their advantages for incompressible high Reynolds number generalised Beltrami flows and beyond. *SMAI J. Comput. Math.*, 5:89–129, 2019.

[18] Vivette Girault and Pierre-Arnaud Raviart. *Finite element methods for Navier–Stokes equations*, volume 5 of *Springer Series in Computational Mathematics*. Springer, 1986.

[19] Johnny Guzmán and Michael Neilan. Conforming and divergence-free Stokes elements in three dimensions. *IMA J. Numer. Anal.*, 34(4):1489–1508, 2013.

[20] Johnny Guzmán and Michael Neilan. Conforming and divergence-free Stokes elements on general triangular meshes. *Math. Comput.*, 83(285):15–36, 2014.

[21] Johnny Guzmán and Michael Neilan. Inf-sup stable finite elements on barycentric refinements producing divergence-free approximations in arbitrary dimensions. *SIAM J. Numer. Anal.*, 56(5):2826–2844, 2018.

[22] Ralf Hiptmair, Lingxiao Li, Shipeng Mao, and Weiying Zheng. A fully divergence-free finite element method for magnetohydrodynamic equations. *Math. Models Methods Appl. Sci.*, 28(4):1–37, 2018.

[23] Qingguo Hong, Fei Wang, Shuonan Wu, and Jinchao Xu. A unified study of continuous and discontinuous Galerkin methods. *Sci. China, Math.*, 62(1):1–32, 2019.

[24] Kaibo Hu, Yicong Ma, and Jinchao Xu. Stable finite element methods preserving $\nabla \cdot \mathbf{B} = 0$ exactly for MHD models. *Numer. Math.*, 135(2):371–396, 2017.

[25] Kaibo Hu and Jinchao Xu. Structure-preserving finite element methods for stationary MHD models. *Math. Comput.*, 88(316):553–581, 2019.

[26] Yunqing Huang and Shangyou Zhang. A lowest order divergence-free finite element on rectangular grids. *Front. Math. China*, 6(2):253–270, 2011.

[27] Volker John, Alexander Linke, Christian Merdon, Michael Neilan, and Leo G. Rebholz. On the divergence constraint in mixed finite element methods for incompressible flows. *SIAM Rev.*, 59(3):492–544, 2017.

[28] Guzmán Johnny and Neilan Michael. A family of nonconforming elements for the Brinkman problem. *IMA J. Numer. Anal.*, 32(4):1484–1508, 2012.

[29] Reijo Kouhia and Rolf Stenberg. A linear nonconforming finite element method for nearly incompressible elasticity and Stokes flow. *Comput. Methods Appl. Mech. Eng.*, 124(3):195–212, 1995.

[30] Alexander Linke and Christian Merdon. Well-balanced discretisation for the compressible Stokes problem by gradient-robustness. In *Finite Volumes for Complex Applications IX - Methods, Theoretical Aspects, Examples*, volume 323 of *Springer Proceedings in Mathematics & Statistics*, pages 113–121. Springer, 2020.

[31] Alexander Linke and Leo G. Rebholz. Pressure-induced locking in mixed methods for time-dependent (Navier–) Stokes equations. *J. Comput. Phys.*, 388:350–356, 2019.

[32] Kent Andre Mardal, Xue-Cheng Tai, and Ragnar Winther. A robust finite element method for Darcy–Stokes flow. *SIAM J. Numer. Anal.*, 40(5):1605–1631, 2002.

[33] Michael Neilan and Duygu Sap. Stokes elements on cubic meshes yielding divergence-free approximations. *Calcolo*, 53(3):263–283, 2016.

[34] Jinshui Qin and Shangyou Zhang. Stability and approximability of the $P_1 - P_0$ element for Stokes equations. *Int. J. Numer. Methods Fluids*, 54(5):497–515, 2007.

[35] Philipp W. Schroeder and Gert Lube. Divergence-free $H(\mathrm{div})$-FEM for time-dependent incompressible flows with applications to high Reynolds number vortex dynamics. *J. Sci. Comput.*, 75(2):830–858, 2018.

[36] Larkin R. Scott and Michael Vogelius. Norm estimates for a maximal right inverse of the divergence operator in spaces of piecewise polynomials. *RAIRO, Modélisation Math. Anal. Numér.*, 19(1):111–143, 1985.

[37] Rolf Stenberg. A technique for analysing finite element methods for viscous incompressible flow. *Int. J. Numer. Methods Fluids*, 11(6):935–948, 1990.

[38] Xue-Cheng Tai and Ragnar Winther. A discrete de Rham complex with enhanced smoothness. *Calcolo*, 43(4):287–306, 2006.

[39] Shinya Uchiumi. A viscosity-independent error estimate of a pressure-stabilized Lagrange-Galerkin scheme for the Oseen problem. *J. Sci. Comput.*, 80(2):834–858, 2019.

[40] Xiaoping Xie, Jinchao Xu, and Guangri Xue. Uniformly stable finite element methods for Darcy–Stokes–Brinkman models. *J. Comput. Math.*, 26(3):437–455, 2008.

[41] Jinchao Xu. Iterative methods by space decomposition and subspace correction. *SIAM Rev.*, 34(4):581–613, 1992.

[42] Xuejun Xu and Shangyou Zhang. A new divergence-free interpolation operator with applications to the Darcy–Stokes–Brinkman equations. *SIAM J. Sci. Comput.*, 32(2):855–874, 2010.

[43] Shangyou Zhang. A new family of stable mixed finite elements for the 3D Stokes equations. *Math. Comput.*, 74(250):543–554, 2005.

[44] Shangyou Zhang. On the P_1 Powell–Sabin divergence-free finite element for the Stokes equations. *J. Comput. Math.*, 26(3):456–470, 2008.

[45] Shangyou Zhang. Divergence-free finite elements on tetrahedral grids for $k \geqslant 6$. *Math. Comput.*, 80(274):669–695, 2011.

[46] Shangyou Zhang. Quadratic divergence-free finite elements on Powell–Sabin tetrahedral grids. *Calcolo*, 48(3):211–244, 2011.

[47] Shangyou Zhang. A family of $Q_{k+1,k} \times Q_{k,k+1}$ divergence-free finite elements on rectangular grids. *SIAM J. Numer. Anal.*, 47(3):2090–2107, 2090.